


# Clinical and molecular features of acquired resistance to immunotherapy in non-small cell lung cancer

## Journal Article

### Author(s):

Memon, Danish; Schoenfeld, Adam J.; Ye, Darwin; Fromm, George; Rizvi, Hira; Zhang, Xiang; Keddar, Mohamed Reda; Mathew, Divij; Yoo, Kyung Jin; Qiu, Jingya; Lihm, Jayon; Miriyala, Jayalaksmi; Sauter, Jennifer L.; Luo, Jia; Chow, Andrew; Bhanot, Umesh K.; McCarthy, Caroline; Vanderbilt, Chad M.; Liu, Cailian; Abu-Akeel, Mohsen; [Beltrao, Pedro](#)  et al.

### Publication date:

2024-02-12

### Permanent link:

<https://doi.org/10.3929/ethz-b-000659404>

### Rights / license:

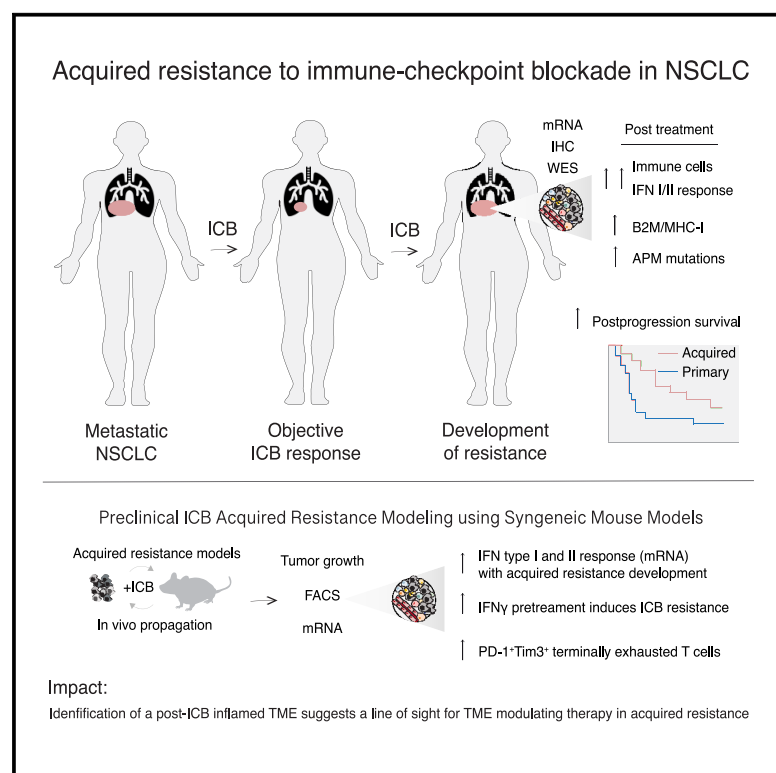
[Creative Commons Attribution-NonCommercial 4.0 International](#)

### Originally published in:

Cancer Cell 42(2), <https://doi.org/10.1016/j.ccell.2023.12.013>

# Clinical and molecular features of acquired resistance to immunotherapy in non-small cell lung cancer

## Graphical abstract



## Authors

Danish Memon, Adam J. Schoenfeld, Darwin Ye, ..., Andy J. Minn, Martin L. Miller, Matthew D. Hellmann

## Correspondence

andyminn@upenn.edu (A.J.M.), martin.miller.publications@gmail.com (M.L.M.), hellmanm@mskcc.org (M.D.H.)

## In brief

Memon et al. demonstrate the relationship between persistent and upregulated interferon signaling and acquired resistance in tumors from patients with NSCLC who have developed acquired resistance to PD-(L)1 blockade. These findings inform approaches for overcoming acquired resistance, which occurs in >60% of patients with NSCLC who initially respond to PD-(L)1 blockade.

## Highlights

- >60% of initial responders to ICBs with stage IV NSCLC acquire resistance (AR)
- AR tumors had upregulated or stable expression of IFN $\gamma$  response genes
- An AR inflammatory phenotype can be recapitulated in multiple murine models
- Altered, persistent inflammation informs strategies to overcome AR to ICB in NSCLC



## Article

# Clinical and molecular features of acquired resistance to immunotherapy in non-small cell lung cancer

Danish Memon,<sup>1,2,3,28</sup> Adam J. Schoenfeld,<sup>4,5,28</sup> Darwin Ye,<sup>6,7,8,9,28</sup> George Fromm,<sup>10,28</sup> Hira Rizvi,<sup>11,12,28</sup> Xiang Zhang,<sup>13</sup> Mohamed Reda Keddar,<sup>14</sup> Divij Mathew,<sup>8,15,16</sup> Kyung Jin Yoo,<sup>10</sup> Jingya Qiu,<sup>6,7,8,9</sup> Jayon Lihm,<sup>17</sup> Jayalaksmi Miriyala,<sup>10</sup> Jennifer L. Sauter,<sup>18</sup> Jia Luo,<sup>4</sup> Andrew Chow,<sup>4,5</sup> Umesh K. Bhanot,<sup>19</sup> Caroline McCarthy,<sup>11</sup> Chad M. Vanderbilt,<sup>18</sup> Cailian Liu,<sup>20</sup> Mohsen Abu-Akeel,<sup>20</sup> Andrew J. Plodkowski,<sup>21</sup> Nicholas McGranahan,<sup>22</sup> Marta Łuksza,<sup>23</sup> Benjamin D. Greenbaum,<sup>17</sup> Taha Merghoub,<sup>4,5,20,24,25</sup> Ikbel Achour,<sup>26</sup> J. Carl Barrett,<sup>26</sup> Ross Stewart,<sup>26</sup> Pedro Beltrao,<sup>1,27</sup> Taylor H. Schreiber,<sup>10</sup> Andy J. Minn,<sup>6,7,8,9,\*</sup> Martin L. Miller,<sup>2,14,\*</sup> and Matthew D. Hellmann<sup>4,5,12,24,29,\*</sup>

<sup>1</sup>European Molecular Biology Laboratory (EMBL), European Bioinformatics Institute, Wellcome Genome Campus, Hinxton, Cambridge, UK

<sup>2</sup>Cancer Research UK Cambridge Institute, University of Cambridge, Li Ka Shing Centre, Robinson Way, Cambridge, UK

<sup>3</sup>M:M Bio Limited, 99 Park Drive, Milton, Abingdon, UK

<sup>4</sup>Department of Medicine, Memorial Sloan Kettering Cancer Center, New York, NY, USA

<sup>5</sup>Department of Medicine, Weill Cornell Medicine, New York, NY, USA

<sup>6</sup>Department of Radiation Oncology, Perelman School of Medicine, University of Pennsylvania, Philadelphia, PA, USA

<sup>7</sup>Abramson Family Cancer Research Institute, Perelman School of Medicine, University of Pennsylvania, Philadelphia, PA, USA

<sup>8</sup>Parker Institute for Cancer Immunotherapy, Perelman School of Medicine, University of Pennsylvania, Philadelphia, PA, USA

<sup>9</sup>Mark Foundation Center for Immunotherapy, Immune Signaling, and Radiation, University of Pennsylvania, Philadelphia, PA, USA

<sup>10</sup>Shattuck Labs, Durham, NC, USA

<sup>11</sup>Druckenmiller Center for Lung Cancer Research, Memorial Sloan Kettering Cancer Center, New York, NY, USA

<sup>12</sup>Early Clinical Development, Oncology R&D, AstraZeneca, New York, NY, USA

<sup>13</sup>Data Sciences and Quantitative Biology, Discovery Sciences, BioPharmaceuticals R&D, AstraZeneca, Gothenburg, Sweden

<sup>14</sup>Oncology Data Science, Oncology R&D, AstraZeneca, Cambridge, UK

<sup>15</sup>Institute for Immunology and Immune Health, University of Pennsylvania, Perelman School of Medicine, Philadelphia, PA, USA

<sup>16</sup>Department of Systems Pharmacology and Translational Therapeutics, University of Pennsylvania, Perelman School of Medicine, Philadelphia, PA, USA

<sup>17</sup>Computational Oncology, Department of Epidemiology and Biostatistics, Memorial Sloan Kettering Cancer Center, New York, NY, USA

<sup>18</sup>Department of Pathology, Memorial Sloan Kettering Cancer Center, New York, NY, USA

<sup>19</sup>Precision Pathology Center, Memorial Sloan Kettering Cancer Center, New York, NY, USA

<sup>20</sup>Ludwig Collaborative and Swim Across America Laboratory, Memorial Sloan Kettering Cancer Center (MSK), New York, NY, USA

<sup>21</sup>Department of Radiology, Memorial Sloan Kettering Cancer Center, New York, NY, USA

<sup>22</sup>Cancer Genome Evolution Research Group, University College London Cancer Institute, London, UK

<sup>23</sup>Department of Oncological Sciences, Icahn School of Medicine at Mount Sinai, New York, NY, USA

<sup>24</sup>Parker Institute for Cancer Immunotherapy, MSK, New York, NY, USA

<sup>25</sup>Human Oncology and Pathogenesis Program, MSK, New York, NY, USA

<sup>26</sup>Translational Medicine, Oncology R&D, AstraZeneca, Cambridge, UK

<sup>27</sup>Institute of Molecular Systems Biology, ETH Zürich, Zurich, Switzerland

<sup>28</sup>These authors contributed equally

<sup>29</sup>Lead contact

\*Correspondence: [andyminn@upenn.edu](mailto:andyminn@upenn.edu) (A.J.M.), [martin.miller.publications@gmail.com](mailto:martin.miller.publications@gmail.com) (M.L.M.), [hellmanm@mskcc.org](mailto:hellmanm@mskcc.org) (M.D.H.)

<https://doi.org/10.1016/j.ccell.2023.12.013>

## SUMMARY

Although immunotherapy with PD-(L)1 blockade is routine for lung cancer, little is known about acquired resistance. Among 1,201 patients with non-small cell lung cancer (NSCLC) treated with PD-(L)1 blockade, acquired resistance is common, occurring in >60% of initial responders. Acquired resistance shows differential expression of inflammation and interferon (IFN) signaling. Relapsed tumors can be separated by upregulated or stable expression of IFN $\gamma$  response genes. Upregulation of IFN $\gamma$  response genes is associated with putative routes of resistance characterized by signatures of persistent IFN signaling, immune dysfunction, and mutations in antigen presentation genes which can be recapitulated in multiple murine models of acquired resistance to PD-(L)1 blockade after *in vitro* IFN $\gamma$  treatment. Acquired resistance to PD-(L)1 blockade in NSCLC is associated with an ongoing, but altered IFN response. The persistently inflamed, rather than excluded or deserted, tumor microenvironment of acquired resistance may inform therapeutic strategies to effectively reprogram and reverse acquired resistance.



## INTRODUCTION

PD-(L)1 blockade can generate profound, durable responses in patients with lung cancer and has been rapidly incorporated into the treatment paradigm for most patients with advanced non-small cell lung cancer (NSCLC).<sup>1,2</sup> Unfortunately, even among those patients who initially respond to PD-(L)1 blockade, over half will eventually develop progression—termed acquired resistance (AR).<sup>3</sup> Alongside primary resistance (refractory to initial treatment), AR represents a significant and possibly underappreciated clinical challenge.<sup>3</sup> Remarkably little is known about the molecular mediators of AR. Perhaps relatedly, effective therapies to circumvent or reverse AR largely remain elusive.

The landscape of immune AR to PD-(L)1 blockade is poorly understood. By contrast, several molecular mechanisms of AR to molecularly targeted therapies (e.g., EGFR and ALK-directed tyrosine kinase inhibitors) have been identified and led to significant therapeutic advances.<sup>1,2</sup> In patients with lung cancer treated with PD-(L)1 blockade, there have been a few published cases of AR.<sup>4–10</sup> Along with case reports in other diseases, these studies have identified that loss of key proteins associated with antigen presentation (AP) or defects of the interferon- $\gamma$  (IFN $\gamma$ ) signaling pathway can contribute to immune resistance.<sup>8,11–13</sup> Pre-clinical work has further highlighted how the relative acuity vs. chronicity of IFN $\gamma$  exposure can contribute to immune dysfunction and tumor resistance.<sup>14–16</sup> Improved understanding of the nature and biology underlying AR is imperative to develop more effective next-generation immunotherapies in the future.

To address the clinical and molecular landscape of AR to PD-(L)1 blockade in patients with NSCLCs, we examined a large clinical cohort ( $n = 118$  out of 1,201 analyzed in the study) of AR to PD-(L)1 blockade in lung cancer paired with a systematic genomic and transcriptomic analysis in a subset of patients ( $n = 29$ ) with available tissue samples. We then also examined several isogenically paired murine models of initially sensitive vs. late relapse derived resistant tumor lines to PD-(L)1 blockade to validate relationships identified in human samples.

## RESULTS

### AR to PD-1 blockade in NSCLC is common

Of 1,201 patients with NSCLC treated with PD-1 blockade at Memorial Sloan Kettering Cancer Center (MSK) between April 2011 through December 2017, 243 (20%) achieved initial response. Many patients who responded ultimately developed AR, with an estimated cumulative AR rate of 61% (95% CI 36%–85%) at 5 years of follow up using a competing risk model (Figure 1A). The onset of AR was variable (52% within 1 year, 39% 1–2 years, 11% > 2 years) (Figure 1B). The relative risk of developing AR decreased with longer duration of initial response (Figure 1C).

Although AR and primary resistance have not been directly compared previously, we hypothesize that these scenarios are distinct biologically and clinically. Consistent with this, we found that several baseline clinical features differed between patients with AR and primary resistance (Figure 1D). High tumor PD-L1 protein expression in baseline (pre-treatment) tissue, in particular, was enriched among patients with AR compared to primary resistance (55% vs. 28%, Fisher's  $p = 0.02$ ). The organ-specific pattern of progression also differed, with liver metastasis being a

common site of progression at primary resistance but relatively uncommon in AR (31% vs. 7%, Odds Ratio 6.23, Fisher's  $p < 0.0001$ , Figure 1E). Perhaps most notably, the post-progression overall survival was significantly longer in patients with AR compared to primary progression (median 18.9 months vs. 4.4 months, log rank  $p < 0.0001$  Figure 1F), potentially suggestive of persistent, partially effective anti-tumor immune responses that permits prolonged survival even after the initial onset of AR. Overall, AR was largely characterized by distinct clinical features, suggesting AR may have underlying immunobiologic features that are distinct from primary resistance and in need of dedicated analysis.

### Patient cohort for molecular profiling of AR to PD-1 blockade

To investigate the molecular mechanisms of AR to PD-1 blockade in patients with NSCLC, we generated microarray-based whole transcriptome expression data, and whole exome sequencing (WES) data from pre- and/or post-treatment tumors in a subset of patients. Patients with analyzed samples had similar baseline characteristics to those in the larger clinical cohort (Table S1). After quality control and sample prioritization, the primary analysis of the molecular data focused on 42 tumor samples (13 pre-treatment, 29 post-treatment) from 29 patients for expression data and 34 tumor samples (15 pre-treatment, 19 post-treatment) from 22 patients for exome data (Figure 2A and Table S2). Thirteen patients had expression data available from both pre- and post-treatment tissue; 12 patients had exome data available from both pre- and post-treatment tissue. All post-treatment samples were obtained following radiographic progression to PD-1 blockade (median time from progression to sample collection 3.7 weeks, interquartile range [IQR] 1.8–10.4) and prior to initiation of new systemic therapy (patients did not receive combination PD-1 blockade with chemotherapy; Figure 2B).

Our work and others<sup>17</sup> have shown that AR frequently occurs in an oligoprogressive pattern, highlighting the importance of assessing the lesion-level response in the analysis of AR. Therefore, we examined the lesion-level response (and resistance) from which each sample was collected to optimize that pre-treatment and post-treatment samples reliably represented the biology of responsive and AR tumors, respectively. Specifically, all post-treatment samples were derived from sites with lesion-specific radiologic rebound growth or *de novo* growth (Figures 2C, S1A, S1B, and S2).

### AR to PD-1 blockade is associated with a distinct transcriptional landscape

Principal components analysis (PCA) of protein-coding gene expression profiles from whole transcriptome data of all 42 samples showed no major technical or clinical factors influenced clustering, including batch and site of sample collection (i.e., lung, lymph node, adrenal, etc) (Figures S3A and S3B). There was also no separation among lesions that were present pre-treatment and later grew compared to those that emerged *de novo* during treatment (Figure S3C). We summarized gene expression values to pathway-level scores using single sample gene set enrichment analysis (ssGSEA)<sup>18</sup> on hallmark<sup>19</sup> gene sets categorized into oncogenic, cellular stress, immune,

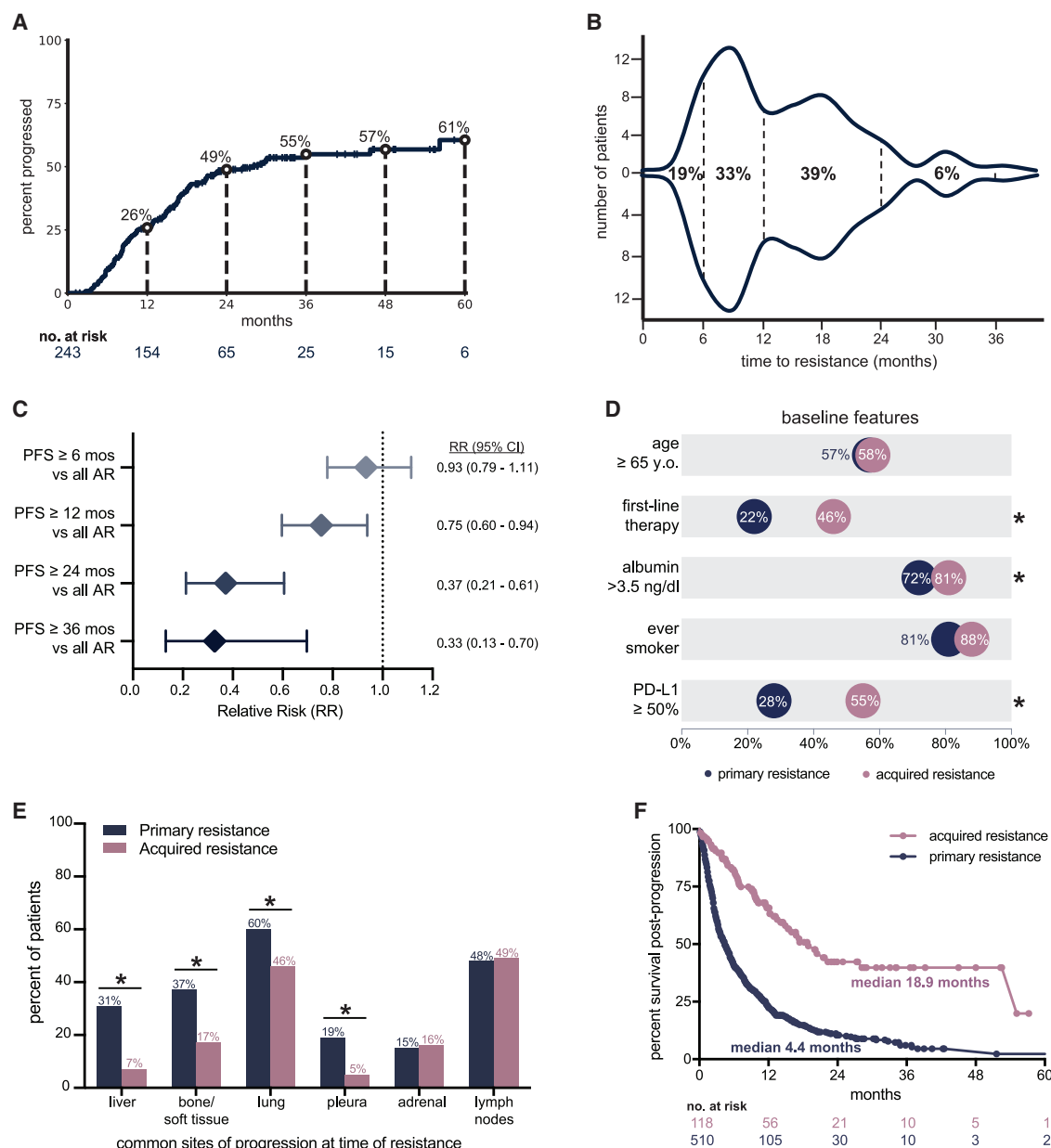


**Figure 1. Clinical features of acquired resistance to immunotherapy in lung cancer**

(A) Cumulative incidence of developing acquired resistance among patients with NSCLC with initial response to PD-1 blockade therapy.

(B) Time to onset of acquired resistance among responders (n = 243).

(C) Estimated rate of developing acquired resistance defined by duration of initial response.

(D) Rates of baseline clinical features among patients with primary (n = 346) and acquired resistance (n = 118). Asterisk represents significant comparisons of Fisher's p < 0.05.

(E) Common organ sites of progression at time of primary or acquired resistance. \* represents significant comparisons of Fisher's p < 0.05.

(F) Post-progression overall survival in patients with primary or acquired resistance (log rank p < 0.0001). See also Table S1.

stromal and other processes as previously applied.<sup>20</sup> PCA clustering of 26 paired samples using enrichment scores (ES) showed a separation of samples based on paired pre- and post-treatment timepoints, with the separation primarily driven by immune-related hallmark gene sets (Figures 3A and 3B). Differential expression analysis of paired samples for hallmark gene sets showed a significant upregulation of IFN alpha/gamma

response, oxidative phosphorylation, and DNA repair pathways after treatment (false discovery rate [FDR] < 0.1, Figure 3C and Table S3). Clustering of paired samples based on computational deconvolution of immune cell estimates from bulk expression derived using CIBERSORT<sup>21</sup> showed a separation of pre- and post-treatment samples particularly driven by infiltration of CD8<sup>+</sup> T cells (Figures 3D and 3E). Significant increase in immune

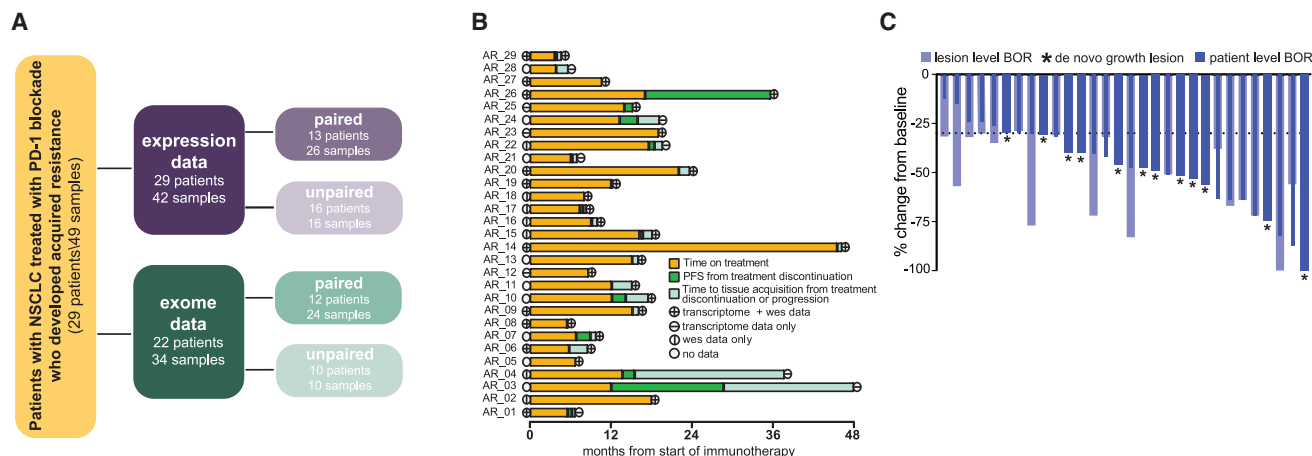


**Figure 2. Overview of the patient cohort used for the exome and expression analyses**

(A) Flow diagram depicting molecular profiling of samples from patients with NSCLC treated with PD-1 blockade who developed acquired resistance. Paired samples are those collected prior to treatment initiation with PD-1 inhibitor and at time of resistance from the same patient. Unpaired samples include single timepoints of collection; prior to treatment initiation or at time of resistance.

(B) Swimmer's plot of when each patient was molecularly profiled. Course of treatment, progression-free survival, and time to tissue acquisition are depicted. Lines within circles identify the type of sequencing completed.

(C) Waterfall plot of Response Evaluation Criteria in Solid Tumors (RECIST) best overall response in patient (dark blue) and lesion (light blue). Dashed line represents 30% shrinkage. Asterisk represents new metastatic lesions that appeared during treatment and continued to grow consistent with a site of acquired resistance (*de novo* growth). See also Figures S1 and S2; Tables S1 and S2.

infiltration (Wilcoxon signed-rank test  $p < 0.05$ ; Figure S3D) and specifically CD8<sup>+</sup> T cells was also observed post-therapy from differential analysis of paired pre-treatment and post-treatment samples (FDR  $< 0.1$ , Figure 3F and Table S3).

Several clinical and pre-clinical studies have generated bulk or single-cell RNA-seq datasets to identify gene sets associated with immune checkpoint blockade (ICB) resistance and T cell dysfunction. We curated a non-redundant resource of these gene sets plus the hallmark gene sets (hereafter termed Hallmark and ICB resistance gene set, see STAR Methods for details) and compared differential changes among the paired samples (Tables S3 and S4). Among these, comparing post-treatment to pre-treatment samples, we found an increase in expression of AP pathway, IFN $\gamma$ ,<sup>22</sup> CD8 T effectors,<sup>23</sup> and proliferating exhausted CD8<sup>+</sup> T cells,<sup>24</sup> while genes belonging to WNT<sup>25</sup> pathway showed modest reduction in expression (Figure 3G). Consistent with these gene sets associated with ongoing immune response to PD-1 blockade, expression of individual genes enriched in post-treatment tumors included GZMA, B2M, and CXCL9 (Figure 3H and Table S5).

### Chronic and therapy-dependent increase in IFN $\gamma$ response pathway as a potential route to AR to ICB

Given the variability in the time to progression in the patient cohort (Figure 2B), we next applied pseudotime analysis using Phenopath<sup>26</sup> to model disease progression in a continuous “latent” space based on gene expression variability within the cohort (Figure 4A). Using the 500 genes with the largest gene expression variability in pre- and post-treatment samples and subject ID and treatment as covariates, pseudotime scores generally increased from pre- and post-treatment samples, in particular, for a group of patients with low pre-treatment pseudotime estimates (Figure 4B). To identify pathways that potentially

are associated with AR, we performed correlation analysis between change in pseudotime and change in pathway ssGSEA ES and signatures using the Hallmark and ICB resistance gene set compendium (Figure 4C). Among the top 10 positively correlated pathways with pseudotime, several IFN type I and II (IFN $\gamma$ ) signatures were correlated significantly, including IFN-stimulated genes (ISGs) that comprise the IFN $\gamma$  hallmark gene set (Figure 4D, FDR  $< 0.01$ ). Notably, samples could be separated into two subsets, with about half of samples showing little to no increase pre- to post-treatment and the other half characterized by elevated expression in ISGs related to an IFN $\gamma$  response. This led us to categorize the patients into an IFN $\gamma$  response “stable” and an IFN $\gamma$  response “increase” group (Figures 4D and 4E).

As sustained cancer-intrinsic IFN signaling has been linked to ICB resistance in pre-clinical mouse models of melanoma and other cancers, we tested whether the change in ISG signatures (IFN $\alpha$  and IFN $\gamma$  hallmark gene sets) observed in our clinical cohort related to a resistance signature derived from an ICB-resistant mouse model of melanoma.<sup>15,27</sup> We found a significant association between the mouse-derived ICB resistance signature and the treatment-induced change in IFN $\gamma$  response (Spearman's rank correlation  $r = 0.90$ ;  $p = 2.2 \times 10^{-16}$ ; Figure 4F), which persisted after removing overlapping genes ( $r = 0.86$ ;  $p = 0.0003$ ). Separately, PCA of change in enrichment score of hallmark gene sets between paired lesions showed a separation of patients on the 1st principal components based on the extent of change of ISG signatures (Figures S4A–S4C). The correlation was significantly stronger for change in the IFN $\gamma$ -related ISGs ( $r = 0.9$ ;  $p < 2.2 \times 10^{-16}$ ) when compared to change in IFN $\alpha$ -related ISGs ( $r = 0.48$ ;  $p = 0.09$ ; Figures S4D and S4E).

Consistent with a differential change of IFN $\gamma$  response genes in these patients, tumors with an increase in IFN $\gamma$ -related ISGs



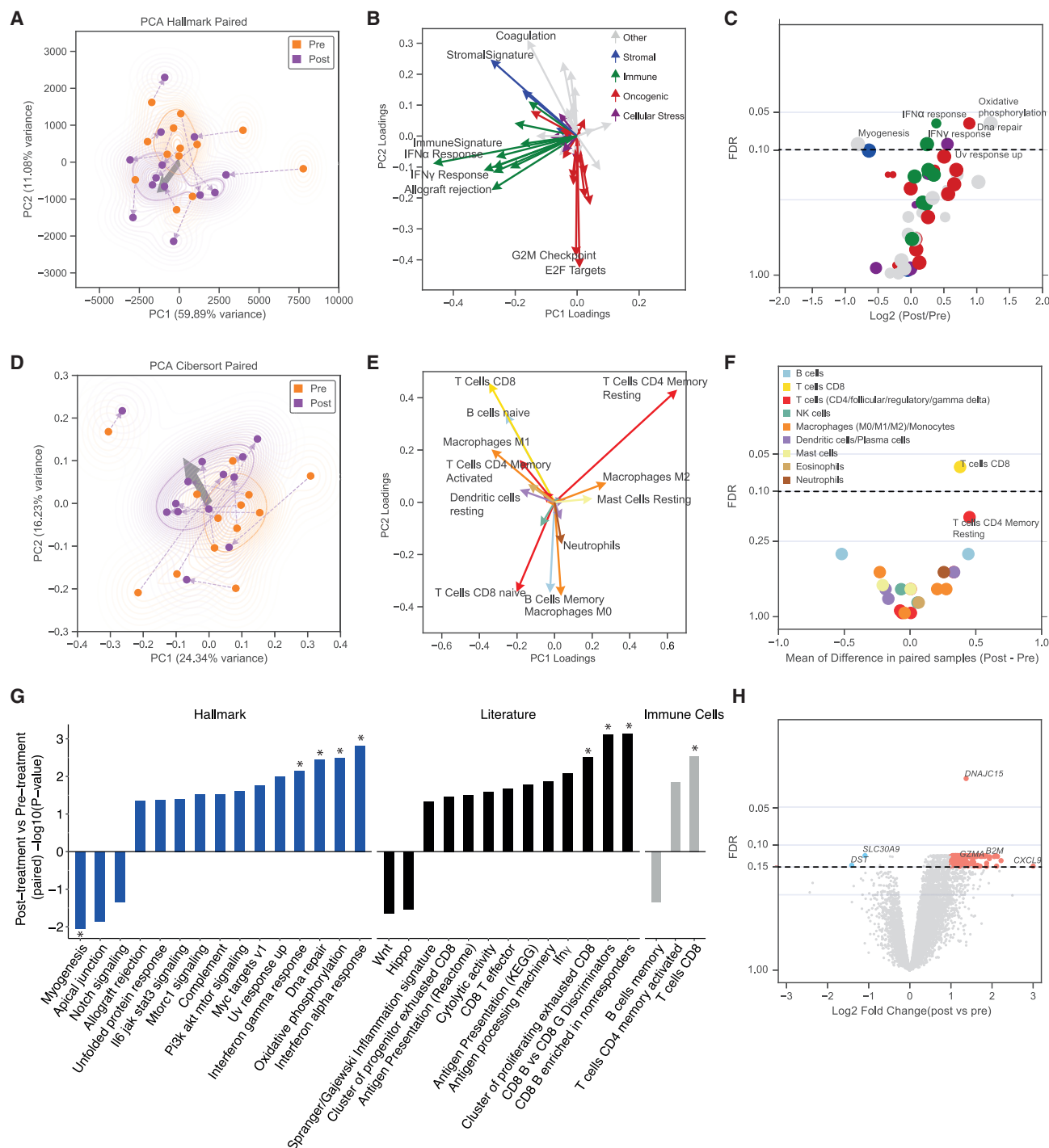


**Figure 3. Resistant lesions show up-regulation of IFN $\gamma$  response pathway and infiltration of CD8 $^{+}$  T cells**

(A) Principal components analysis of paired samples using enrichment scores of hallmark gene sets derived from ssGSEA. Paired pre- and post-treatment lesions from the same patient are connected using a dashed line ( $n = 26$ ). The light gray arrow indicates the average directionality of change for each pair.

(B) Principal components feature loadings of hallmark gene sets with both magnitude and direction. Biological processes in hallmark gene sets were categorized into sub-groups as previously described<sup>20</sup> and colour-coded accordingly.

(C) Differential comparison of hallmark enrichment scores between pre- and post-treatment samples. Each point represents a hallmark gene set and point size indicates the number of genes in a gene set. The x axis indicates the change in hallmark enrichment scores for paired samples from each patient (Post vs. Pre) and the y axis is false discovery rate (FDR)-adjusted p value derived from the comparison of enrichment scores of hallmark gene sets using paired t-test. The black dashed line represents FDR cutoff to identify significant gene sets (FDR < 0.1).

(D) Principal components analysis of immune cell estimates derived using CIBERSORT immune cell deconvolution approach.

(legend continued on next page)

generally had an increase in inferred activity of individual transcription factors associated with activation of ISGs, *STAT1* and *IRF1*, as well as immune signatures (estimated by hallmark and literature gene sets) associated with CD8<sup>+</sup> T cell exhaustion across several studies<sup>24,28</sup> (Figures 4G–4J and Table S6). In addition to signatures of T cell exhaustion, an increase in regulatory T cells<sup>28</sup> was also noted. FOXP3 was specifically upregulated in samples from the subgroup with an “increase” in IFN $\gamma$ -related genes (paired t test  $p = 0.005$ ; Figure S4F). In contrast, patients with “stable” expression of IFN $\gamma$ -related genes were characterized by a lack of change in these immune-related pathways and genes (Table S6). Together these data suggest a recurrent pattern of AR to PD-1 blockade in NSCLC is associated with activation of an IFN $\gamma$  transcriptional program in tumors, presumptive alteration in tumor-specific IFN $\gamma$  signaling (given persistent tumor growth clinically), and a concomitant increase in exhaustion of CD8<sup>+</sup> T cells in the microenvironment.

### Positive selection pressure for antigen presentation gene mutations in AR

To examine somatic alterations and potential mechanisms of AR, we next evaluated the exome sequencing data pre- vs. post-treatment for 12 patients (24 samples with germline single nucleotide polymorphisms [SNPs] confirming paired samples belonged to the same patient; Figure S5A). NSCLC is characterized by a high mutation burden, a strong predictor of response to immunotherapy.<sup>29–31</sup> Overall, there was no significant difference in tumor mutation burden (Wilcoxon signed-rank test  $p = 0.6$ ; Table S7), known driver genes,<sup>32</sup> neoantigen burden, fitness (Wilcoxon signed-rank test  $p = 0.74$ ), or tumor heterogeneity (Wilcoxon signed-rank test  $p = 0.37$ ) before versus after immunotherapy treatment at a summary level (Figures 5A, S5B, and S5C). However, there was evidence of remodeling of clonal or sub-clonal structure in seven patient samples. For five of these patient samples, clonal mutations were retained while a subset of sub-clonal mutations were lost and/or new sub-clonal mutations were also acquired (Figures 5B and S5D). For two patients (AR\_20 and AR\_27), post-treatment lesions did not share any somatic mutations with their respective pre-treatment lesions indicative of emergence of a potentially new tumor or outgrowth of a rare (i.e., below the limit of detection by WES) pre-existing tumor clone (Figure S5E). Among the clonal mutations detected in the post-treatment lesion of AR\_20 included a nonsense mutation in the *STK11* gene consistent with previous observations of an association between mutations in *STK11* and resistance to ICB in lung adenocarcinoma.<sup>33</sup> Several mutational processes, including extrinsic factors, particularly smoking, can influence somatic molecular profile in NSCLC and can be detected as mutational signatures.<sup>34</sup> The smoking signature was the domi-

nant signature in pre-treatment lesions and these mutations persisted in post-treatment lesions. However, post therapy the clonal composition of these tumors had changed potentially shaped by different sets of factors indicated by depleted proportion of smoking related mutations (Figure S5F). Recent studies have shown an enrichment of APOBEC mutational signature in samples from patients who benefit from immunotherapy treatment.<sup>35</sup> In two patients, AR\_08 and AR\_20, we observed a noticeable increase in fraction of private mutations contributing to APOBEC mutational signatures 2 and 13 in the post-treatment lesions (48.3% in AR\_08 and 14.3% in AR\_20) relative to those in the pre-treatment lesions (5.4% in AR\_08 and 1.6% in AR\_20).

Given previous studies describing loss of *B2M* and other genes such as *TAP1*, *TAP2*, and *TAPBP* involved in AP pathway as a potential mechanism of immune escape in resistant tumors, we performed an unbiased analysis to evaluate positive selection pressure on individual genes before and after therapy.<sup>36</sup> As expected, canonical driver mutations in lung cancer such as *KRAS* and *TP53* were under strong positive selection pressure, and there were no recurrently altered driver genes with significant enrichment in post-treatment tumors compared to pre-treatment (Figures 5C and S5G). However, a nonsense mutation and a frameshift deletion in *B2M* were exclusively identified in post-treatment tumors of AR\_14 and AR\_19 respectively, and other immune-related genes such as *IL21R*, *PDCD5*, *FKBP1A*, and *FNIP1* were indeed enriched post-therapy (Figures 5C, S5H, and S5I). No potential pathogenic mutations were observed in *TAP1*, *TAP2*, and *TAPBP* genes.

Given the selective identification of mutations in *B2M* and other immune-related genes in the ICB-resistant tumor samples, we evaluated additional gene sets involved in AP pathways using the GSEA approach. Specifically, we asked whether there was evidence of an association between IFN $\gamma$  selective pressure and dysregulation of AP pathways (Figure 5D). Overlaying mutational changes with IFN $\gamma$  status for the cases with both expression and mutation data, we observed mutation enrichment in the AP pathway to be more common among patient samples that show an “increase” in IFN $\gamma$  response in contrast to those with “stable” IFN $\gamma$  response pathway. Notably, three out of four patient samples with significant change in clonal or sub-clonal architecture (AR\_20, AR\_27, AR\_19), also showed presence of new mutations in the AP pathway genes in their post-treatment lesions (Figure 5E). All four of these patients (AR\_20, AR\_27, AR\_19, AR\_26) also had available tissue for B2M and class 1 HLA protein expression testing on tumor cells and all were negative or decreased from baseline (Figures 5F and 5G).

To explore expression patterns of AR in an independent cohort, we analyzed RNA-seq data from primary and metastatic tumor samples obtained prior to enrollment onto a phase 1b study of durvalumab in combination with tremelimumab in subjects with

(E) Principal components feature loadings of immune cell estimates.

(F) Differential comparison of immune cell estimates (CIBERSORT) between pre- vs. post-treatment samples. Each point represents an immune cell type and associated color reference indicated in panel e. The x axis indicates the change in immune cell estimates for paired samples from each patient (Post vs. Pre) and y axis is FDR adjusted p value derived from paired comparison of immune cell estimates.

(G) Summary of key changes in hallmark gene sets, immune checkpoint blockade-resistance related gene signatures and estimates of immune cells using differential analysis of expression data. All gene sets with p value <0.05 are shown. \* indicates gene sets that were significant after FDR correction (FDR <0.1).

(H) Differentially expressed genes between pre- and post-treatment samples. The black dashed line represents FDR cutoff to identify significant genes (FDR < 0.15). Benjamini-Hochberg (BH) method was used for FDR correction. See also Figure S3 and Tables S3, S4, and S5.



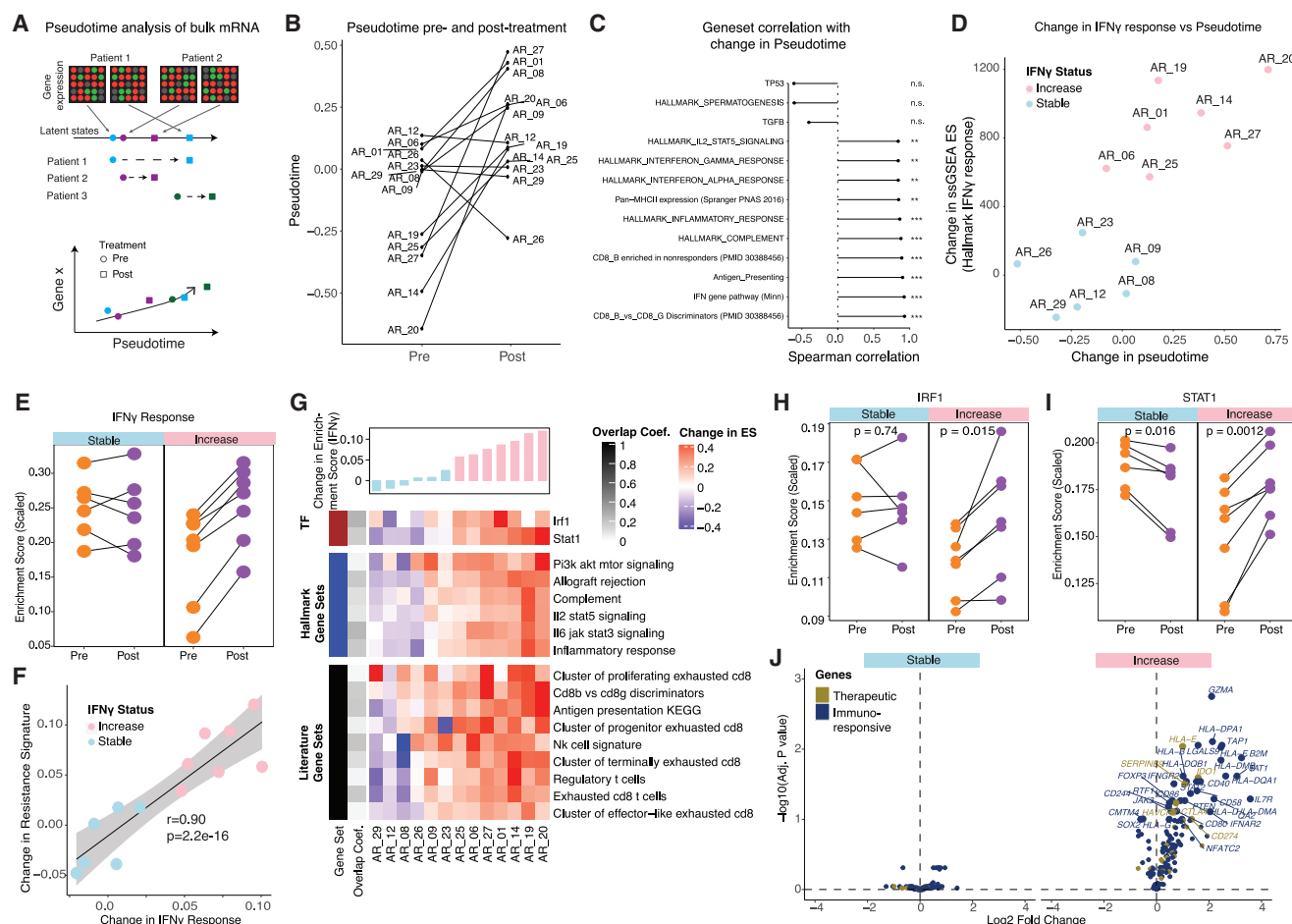


**Figure 4. A subset of samples from patients with acquired resistance have elevated IFN $\gamma$  response and T cell exhaustion signatures post-treatment**

(A) Schematics of pseudotime analysis of bulk mRNA aiming to uncover temporal information that traces the underlying biological process of samples from a cross-sectional cohort of individuals. This analysis assumes that tumors in the cross-sectional cohort behave asynchronously and each patient's sample is at a different stage of progression captured along the trajectory of pre- and post-treatment.

(B) Pseudotime estimates based on the 500 most variable genes in pre- and post-treatment samples using PhenoPath.<sup>26</sup>

(C) Spearman's rank correlation score between change in pseudotime pre- to post-treatment vs. change in ssGSEA-based enrichment scores of the hallmark and immune checkpoint blockade (ICB) resistance gene sets. Top ten positively and top three negatively correlated gene sets are shown. \*\*FDR < 0.01, \*\*\*FDR < 0.001.

(D) Scatterplot of change in ssGSEA enrichment score vs. change in pseudotime estimates pre- to post-treatment with indication of patient samples separating into an IFN $\gamma$  response increase (pink) vs. stable (light blue) group.

(E) Patient samples were sub-divided into "stable" and "increase" categories based on the magnitude of change in the IFN $\gamma$  response signature between the pre- and post-treatment samples.

(F) Correlation between change in the IFN $\gamma$  response signature and change in the ICB-resistance signature derived from a mouse model of melanoma for the paired samples.<sup>27</sup> The change in resistance signature was compared to the change in IFN gamma response using a Spearman's rank correlation.

(G) Change in enrichment scores of key differentially regulated gene sets in either "stable" or "increase" patient samples (pearson correlation  $p < 0.05$ ) ordered according to change in enrichment score of IFN $\gamma$  response signature. The extent of overlap between IFN $\gamma$  response signature and each differentially regulated gene set is represented as the overlap coefficient.

(H and I) Activity of IFN $\gamma$  response associated transcription factors (H) IRF1 and (I) STAT1 in pre- and post-treatment timepoints of patient samples ( $n = 26$ ) in "stable" and "increase" sub-groups.

(J) Differential change in expression levels of previously reported immune-responsive genes and resistance associated therapeutic targets in literature in the "stable" or "increase" sub-group. Benjamini-Hochberg (BH) method was used for  $p$  value adjustment. Statistical comparisons in (H) and (I) were performed using two-tailed paired  $t$  test. See also Figure S4 and Table S6.

advanced NSCLC ("Study 06", NCT02000947). Patients enrolled in the Study 06 trial were either naive to ICB treatment or failed on a previous line of anti-PD-(L)1 monotherapy. Those who failed to respond were further categorized as ICB primary resistant or

ICB AR (Figure 5H). Patients with primary resistance had documented radiographic disease progression  $\leq 16$  weeks from the start of treatment with no evidence of clinical benefit. Patients with AR had radiographic disease progression following initial

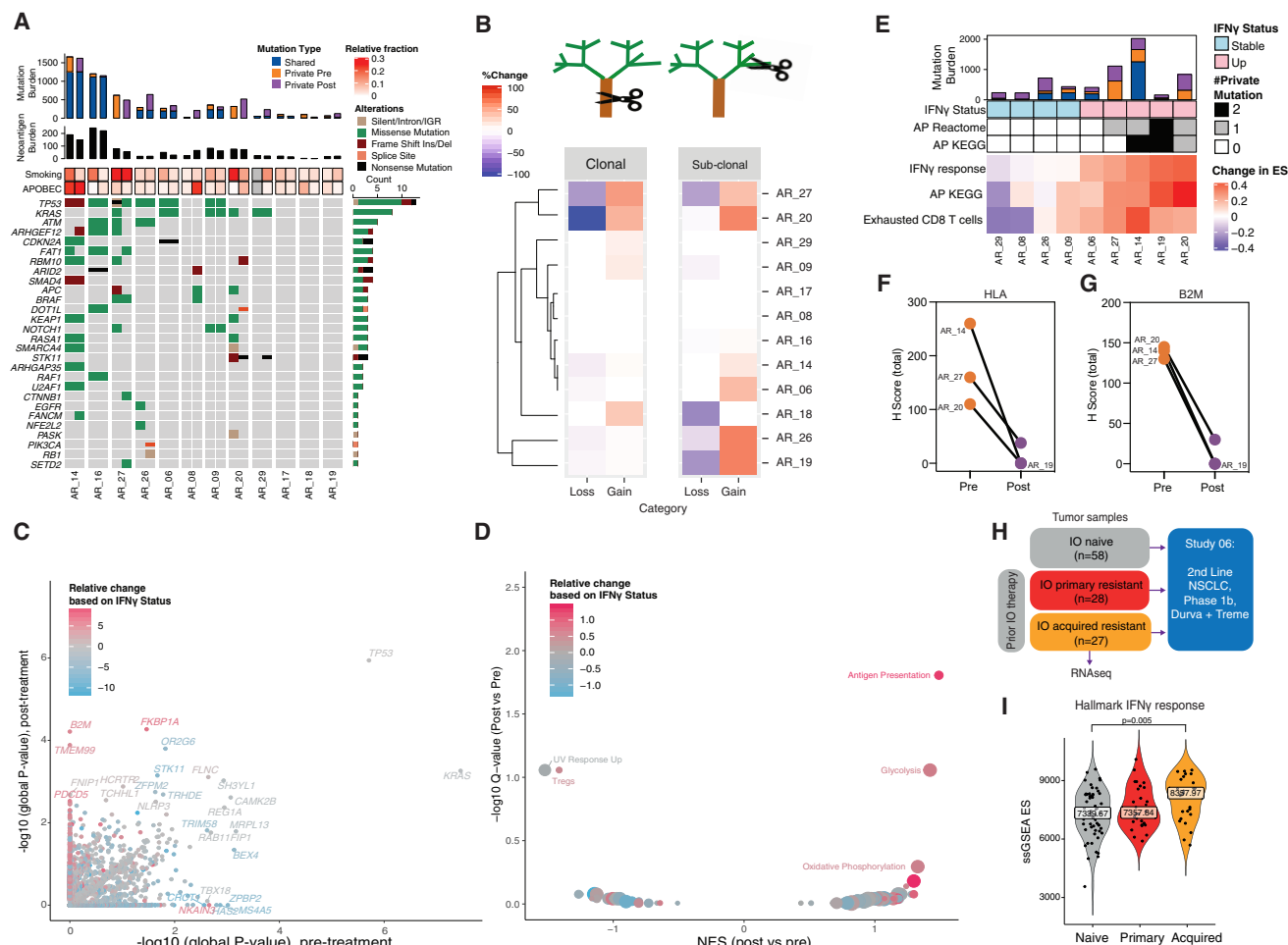


**Figure 5. Genomic dynamics in acquired resistance to PD-1 blockade in lung cancer**

(A) Summary of somatic mutations (missense and indels) in samples from our immune checkpoint blockade (ICB)-resistance cohort for known driver genes in non-small cell lung cancer (NSCLC). Pattern of mutations of recurrently mutated genes derived from a previous study.<sup>32</sup> The heatmap also indicates the unique and shared mutations in each sample and the proportion of mutations associated with key somatic signatures (smoking and APOBEC) associated with lung cancer.

(B) Percentage loss or gain of clonal and sub-clonal mutations in paired samples (n = 24) from each patient.

(C) Comparison of global p value estimates for genes (n = 20,091) derived from dN/dS analysis of missense, truncations and indels to evaluate gene-level selection pressure in pre- and post-treatment samples estimated using dndscv method.<sup>36</sup>

(D) Comparison of global p value estimates genes to identify gene sets under positive selection in pre- and post-treatment samples. The change in gene level global p value between pre- and post-treatment samples (shown in (C)) was used to order genes and estimate GSEA normalized enrichment score and p value for each gene set.

(E) Summary of key changes in expression and mutations in nine patients with pre- and post-treatment measurements for both expression and exome. The private mutations in post-treatment lesions of patients in genes part of antigen presentation pathway (KEGG or REACTOME) are shown.

(F and G) Immunohistochemistry based quantification of (F) HLA/MHC-I and (G) B2M. The pre-treatment lesion of patient AR\_19 did not have enough tissue for immunohistochemistry.

(H) Schematics of samples obtained from patients prior enrollment on Study 06—a phase 1b study in advanced NSCLC where patients were treated with durvalumab (Durva) and tremelimumab (Treme) as a second line therapy. Patients enrolled in the Study 06 trial were either naive to immunotherapy (IO) treatment, had progressed without initial objective response (primary resistant), or progressed after an initial objective response (acquired resistant) on a previous line of anti-PD-(L)1 monotherapy.

(I) Violin plot of ssGSEA enrichment scores for the hallmark IFN $\gamma$  response gene set for samples from the three patient groups. ssGSEA enrichment scores of samples from patients with acquired resistance and patients who were ICB naive were compared using Wilcoxon rank-sum test. See also Figure S5, Tables S7 and S8.

clinical benefit (i.e., complete response, partial response, or stable disease on any scan). To investigate expression pattern differences between ICB naive (n = 58) and patients with AR (n = 27), available RNA-seq data were analyzed by ssGSEA using hallmark

and ConsensusTME<sup>37</sup> gene sets to compare expression patterns of cancer-relevant pathways and immune cell infiltration estimated from bulk tumor mRNA. Similar to our pre- vs. post-treatment cohort, samples from patients in Study 06 with AR had

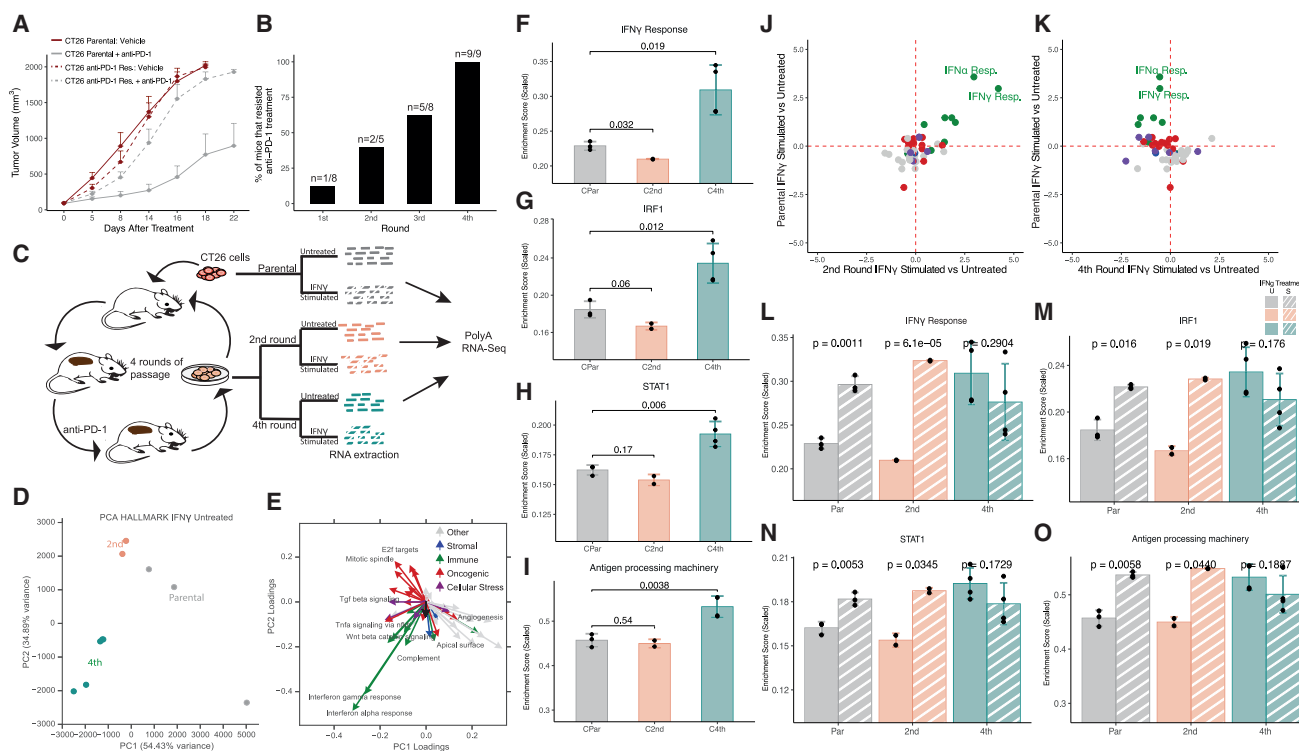


**Figure 6. Cell lines derived from mouse CT26 tumors with acquired resistance to PD-1 show dysfunctional IFN $\gamma$  signaling**

(A) Tumor volume over time after treatment with anti-PD-1 therapy or control (Vehicle) for parental (CT26 parental) and resistant cells (CT26 anti-PD-1 Res.) ( $n = 9$  per group).

(B) Percentage of mice that resisted anti-PD-1 treatment.

(C) Experimental design for development of ICB-resistance model from anti-PD-1 treatment of CT26-derived tumors in mice. Cell lines were derived from tumors and subjected to RNA sequencing.

(D) Principal component analysis (PCA) of IFN $\gamma$ -untreated samples i.e., parental (sensitive), 2nd round and 4th round ICB-resistant cells based on enrichment scores of hallmark gene sets.

(E) Principal components feature loadings of hallmark gene sets with both magnitude and direction. Biological processes in hallmark gene sets were categorized into sub-groups as previously described<sup>20</sup> and the vectors were color-coded accordingly.

(F–I) Enrichment scores in parental, 2nd and 4th round cells for the following genesets: (F) IFN $\gamma$  response pathway, (G) STAT1, (H) IRF1, and (I) antigen processing machinery.

(J) Comparison of significance of change in enrichment score between IFN $\gamma$  stimulated (IFN $\gamma$ s) and IFN $\gamma$  untreated (IFN $\gamma$ u) 2nd round and significance of change in enrichment score between IFN $\gamma$ s and IFN $\gamma$ u parental cells.

(K) Comparison of significance of change in enrichment score between IFN $\gamma$ s and IFN $\gamma$ u 4th round and significance of change in enrichment score between IFN $\gamma$ s and IFN $\gamma$ u parental cells.

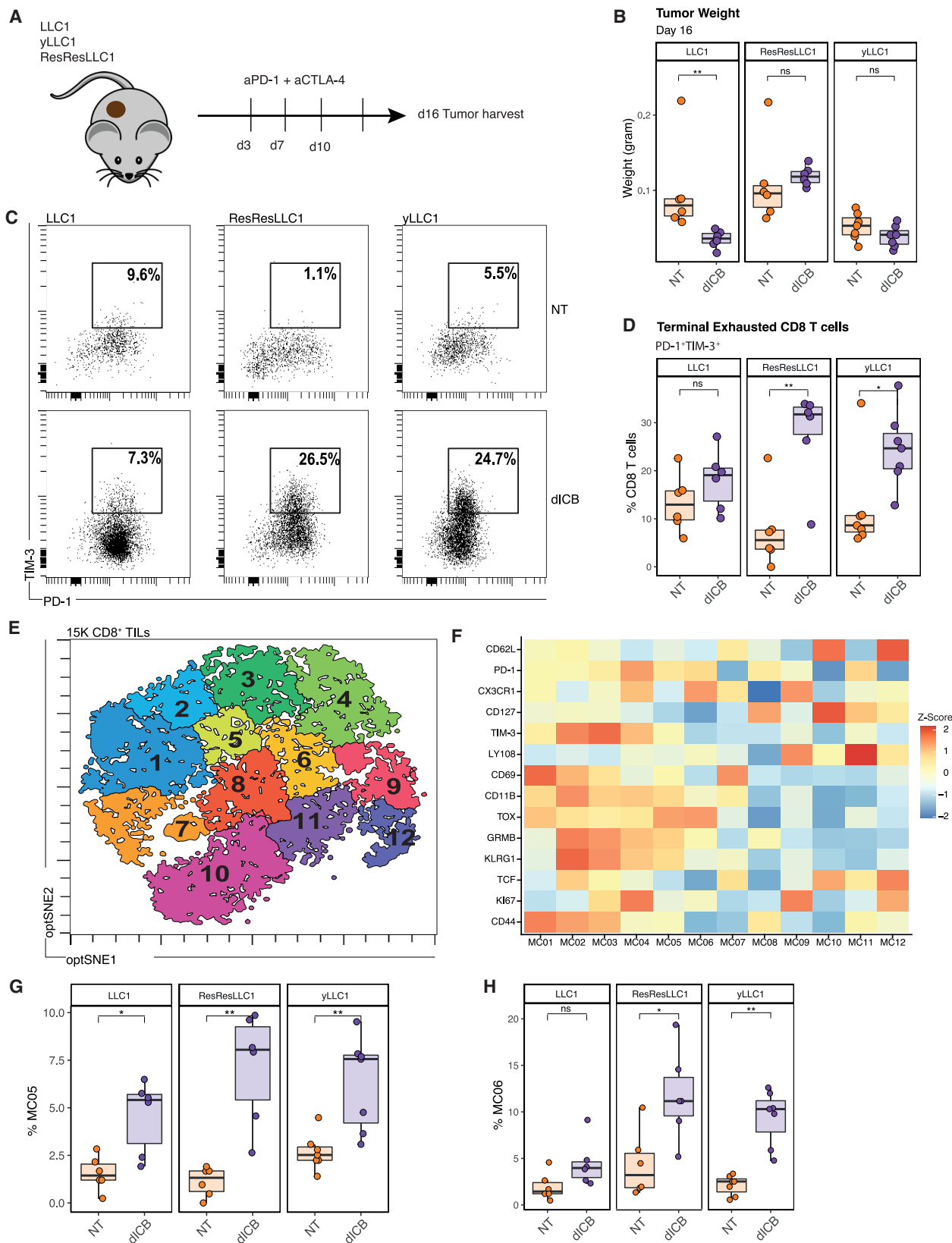
(L–O) Comparison of enrichment scores between IFN $\gamma$ u vs. IFN $\gamma$ s (parental or 2nd or 4th) cells for the following genesets: (L) IFN $\gamma$  response pathway, (M) IRF1, (N) STAT1, and (O) antigen processing machinery. Statistical comparisons in (F), (G), (H), (I), (L), (M), (N), and (O) were performed using unpaired t test. For all panels, error bars are the standard error from the mean. See also Figure S6 and Table S9.

significant enrichment of myeloid cells, T cells, and IFN $\gamma$ -related ISGs compared to treatment naive samples (FDR < 0.05, Figures 5I, S5J, and S5K; Table S8).

### AR is associated with elevated ISGs and alterations in tumor IFN $\gamma$ signaling

To further explore the transcriptional features that are associated with AR to ICB in our clinical cohort, we also examined cancer cell intrinsic transcriptional programs using a pre-clinical murine model system of AR to ICB inhibitors. Similar to PD-1-responsive human lung cancer, the CT26 murine model is carcinogen-induced, has high tumor mutation burden, and is highly sensitive to immunotherapy treatment,<sup>38</sup> and is therefore a well suited pre-clinical analogue for interrogating AR. As expected, subcutane-

ous CT26 tumors showed significant reduction in tumor volume over 3 weeks of anti-PD-1 treatment (Figure 6A). To model AR, persistent viable cells following anti-PD-1 treatment were excised, cultured *in vitro*, and reimplanted in mice. This process was repeated for several passages until CT26 tumors were no longer responsive to anti-PD-1 antibody therapy (Figure 6B). Bulk RNA-seq was performed on the ICB-resistant cancer cell lines derived from tumors from the 2<sup>nd</sup> round ( $n = 2$ ) and 4<sup>th</sup> round ( $n = 4$ ) of *in vivo* passage and compared against the ICB-sensitive parental cell line ( $n = 3$ ; Figure 6C). PCA of whole transcriptome data did not show any clear trend (Figure S6A); however, PCA of hallmark gene sets showed the parental and 2<sup>nd</sup> round samples tend to cluster separately from the 4<sup>th</sup> round samples with the separation mainly driven by IFN alpha/gamma response



(legend on next page)

pathway (Figures 6D and 6E). Systematic comparison of 4<sup>th</sup> round samples with parental samples showed a significant upregulation of IFN $\alpha$  and IFN $\gamma$  response pathway genes (Figures 6F and Table S9). An increase in genes for other biological processes including TNF $\alpha$  signaling (FDR  $\leq$  0.1) and the AP pathway (Figure 6I) were also evident in cells from 4<sup>th</sup> round resistant tumors. In contrast, no significant change in gene sets was observed from the comparison of the 2<sup>nd</sup> round and parental cell lines (Figures S6B and S6C). Similar to the human data, these findings indicate that anti-PD-1 resistance was associated with elevated baseline expression of IFN $\gamma$ -related ISGs.

Alongside the increase in baseline IFN $\gamma$  response pathway genes in the 4<sup>th</sup> round cells, we also observed an increase in the activity of IFN-related transcription factors STAT1 and IRF1 inferred from their regulons (Figures 6G and 6H). Consistent with this increase in transcription factor activity and with our previous findings linking elevated ISGs to epigenetic changes,<sup>39</sup> examination of chromatin accessibility by ATAC-Seq showed enrichment of the JAK-STAT signaling pathway in 4<sup>th</sup> generation anti-PD-1 resistant cells relative to parental cells (q-value < 0.1; Figure S6G) or *in vivo* passaged control cells (q-value < 0.1; Figure S6H). Moreover, an unbiased search for motif sequences in the peaks of promoter regions showed significant enrichment of transcription factor binding motifs for IRF1 in the resistant cells (Figure S6I) but not in parental cells. These findings suggest that enhanced activity of IFN-related transcription factors may contribute to the elevated baseline ISG expression associated with resistant cancer cells.

To explore if ICB resistant cancer cells with elevated ISGs can further induce ISGs after IFN $\gamma$  stimulation, cell lines were stimulated with IFN $\gamma$  for 24 h and compared to unstimulated controls. While the parental and 2<sup>nd</sup> round cell lines showed an increased expression of genes involved in IFN signaling after IFN $\gamma$  stimulation, the 4<sup>th</sup> round cell line did not show an overall induction of ISGs at the transcriptional level (Figures 6J–6L, S6D–S6F, and Table S9). In addition, transcription factors downstream of IFN $\gamma$  signaling, such as STAT1 and IRF1, showed the same pattern with no statistically significant differences in expression between IFN $\gamma$  stimulated vs. control in the 4<sup>th</sup> round cell line (Figures 6M and 6N). As IFN $\gamma$  signaling is known to upregulate AP machinery pathway genes,<sup>40</sup> we also specifically investigated the effect of IFN $\gamma$  on these genes, which further supported the observations and showed no additional induction to IFN $\gamma$  stimulation in 4<sup>th</sup> round cells (Figure 6O).

To examine ISG expression and IFN $\gamma$  response after AR in another well-established immunogenic tumor model, we also analyzed MC38 colorectal carcinoma tumors. Consistent with reports that MC38 is highly responsive to anti-PD-1 treatment with better immunogenicity than the CT26 model<sup>41</sup> (Figure S6J) indeed, subcutaneous MC38 tumors showed significant reduction in tumor volume after three weeks of anti-PD-1 treatment (Figure S6K). Similarly to CT26, we also derived serially progressive MC38 tumors no longer responsive to anti-PD-1 after the 5<sup>th</sup> round (n = 4) of *in vivo* passage. Resistant MC38 cancer cells showed significantly higher levels of multiple ISGs, including *Stat1*, *Stat2*, *Ifitm2*, and *Ifitm3* when compared to parental cells (Figures S6L–S6P). Stimulation with IFN $\gamma$  for 24 h further increased expression; however, compared to parental controls, resistant cells had significantly reduced transcriptional induction for several of these ISGs (Figures S6Q–S6U). Thus, like CT26 tumors, MC38 tumors that relapse after anti-PD-1 are associated with elevated baseline ISGs and develop an altered response to IFN $\gamma$  stimulation. This altered IFN $\gamma$  response could be either a broad insensitivity or a blunted induction for a subset of ISGs.

### Chronic IFN $\gamma$ stimulation of lung cancer cells promotes elevated ISGs, resistance, and immune dysfunction

We previously demonstrated that chronic stimulation of cancer cells with IFN $\gamma$  can be sufficient to render cells resistant to ICB.<sup>14</sup> Moreover, like with the CT26 and MC38 tumors that AR to anti-PD-1, these chronically stimulated cells increase their baseline expression and chromatin accessibility for a subset of ISGs.<sup>39</sup> In order to determine if chronic IFN stimulation is sufficient to render NSCLCs resistant to ICB and also promote T cell dysfunction, we utilized two syngeneic mouse lung cancer models: the *Kras*<sup>lox-stop-lox(Isl)-G12D/+</sup>; *Trp53*<sup>fllox/fllox</sup> (KP) genetically engineered mouse model and the Lewis lung carcinoma (LLC1) (Figures 7A and S7A). With both models, tumors that spontaneously relapsed after ICB were compared to tumors derived from cancer cells that were treated with low levels of IFN $\gamma$  for 3–4 weeks *in vitro* prior to implantation into mice (Figures 7B and S7B). Like KP and LLC1 tumors derived from cells that persist after ICB (ResKP2, ResResKP, ResKPlate, and ResResLLC1), KP and LLC1 tumors from cells exposed to chronic IFN $\gamma$  ( $\gamma$ KP and  $\gamma$ LLC1) were more resistant to ICB and showed increased expression of IFN $\gamma$ -related ISGs, as assessed from cancer cells sorted from untreated tumors (Figure S7C). Tumors associated with chronic IFN signaling either by chronic

**Figure 7. Acquired resistance to immune checkpoint blockade (ICB) associates with induction of terminally exhausted CD8<sup>+</sup> T cells in the LLC1 syngeneic lung cancer mouse model**

(A) Experimental design of anti-PD-1 + anti-CTLA-4 therapy treatment schedule in the LLC1 mouse model following implantation of parental (LLC1), 3–4 weeks IFN $\gamma$  stimulated ( $\gamma$ LLC1) and ICB-resistant LLC1 cell lines.  
(B) Comparison of tumor weights harvested on Day 16 in parental (LLC1), respective tumor types following ICB demonstrated that tumors with chronic IFN features ( $\gamma$ LLC1 and ResResLLC1) do not respond to ICB.  
(C) Representative flow cytometric plots to show the expression of PD-1 and TIM-3 on CD8<sup>+</sup> T cells from non-treated and ICB-treated tumors.  
(D) Comparison of percentage of PD-1<sup>+</sup> TIM-3<sup>+</sup> terminally exhausted CD8 T cells in tumors.  
(E) Unsupervised clustering of CD8 T cell population based on expression of T cell focused immune profiling panel.  
(F) A heatmap to indicate the levels of the different T cell related markers across the 12 meta-clusters, defined of the unsupervised clustering of CD8 T cells.  
(G and H) Comparison of percentage frequency of meta-clusters 5 (MC05) and 6 (MC06) within the CD8 T cell population between non-treated and ICB-treated LLC1,  $\gamma$ LLC1 and ResResLLC1 tumors. The boxplots in (B), (D), (G), and (H) indicate median and the lower and upper hinges correspond to the first and third quartiles. The upper whisker extends from the hinge to the largest value no further than 1.5 \* IQR (inter-quartile range) from the hinge. The lower whisker extends from the hinge to the smallest value at most 1.5 \* IQR of the hinge. Statistical comparisons in (B), (D), (G), and (H) were performed using Wilcoxon rank-sum test. See also Figure S7.



IFN $\gamma$  stimulation *in vitro* for 3–4 weeks ( $\gamma$ LLC1) or a late relapse-derived tumor cell line (ResResLLC1) showed a diminished response to double ICB, a combination of anti-PD-1 + anti-CTLA-4 (Figure 7B). These pre-clinical data confirm our previous finding that high ISGs are associated with progression after ICB in murine tumor models. The diminished ICB efficacy in the LLC1 models harboring chronic IFN signaling ( $\gamma$ LLC1) or late relapse-derived LLC1 tumor cell line (ResResLLC1) are characterized by the accumulation of dysfunctional PD-1<sup>+</sup>TIM-3<sup>+</sup> exhausted T cells in the tumor post-ICB (Figures 7C and 7D). We then systematically characterized the immune infiltrate in the LLC1 tumors (Figures 7E and 7F). Tumor-infiltrating immune cells were categorized into twelve meta-clusters using unsupervised clustering. Interestingly, meta-clusters 5 and 6, that were dominant for T cell exhaustion markers (PD-1<sup>+</sup>, TIM-3<sup>+</sup>, etc.), showed an increase in frequency post-ICB in the chronically IFN stimulated or late relapsed tumor samples, but not in the initially sensitive tumor samples (Figures 7G, 7H, and S7D).

## DISCUSSION

Although PD-1 blockade has been transformative in the treatment of patients with NSCLC, AR is common and understanding of the molecular mechanisms of resistance remains quite limited. Before embarking on this report, we had hypothesized that “non-inflamed” or “cold” tumors, characterized by exclusionary immunologic barriers or an absence of T cell infiltration, would significantly contribute to resistance.<sup>3</sup> Previously, neoantigen loss and tumor-mediated immunosuppression have been associated with primary resistance to immunotherapy.<sup>5,42,43</sup> In contrast, we found that neoantigen depletion does not appear to be a dominant mediator of AR. In fact, most tumors have retained or increased inflammatory characteristics, rather than immune excluded or desert phenotype, with significant upregulation of IFN $\gamma$  suggestive of persistent, but evidently insufficient anti-tumor immune response. The persistent, if incomplete, anti-tumor immune response may also manifest in the clinical observation that some patients who develop AR can still have durable survival for many years following initial emergence of resistance. In addition to associations with chronic upregulation of the IFN $\gamma$  response pathway, we also observed strong upregulation of oxidative phosphorylation and DNA repair pathway genes which are consistent with a recent report<sup>44</sup> which proposes acquisition of a hypermetabolic state with high expression of glycolytic and oxidative phosphorylation pathway genes as a potential escape mechanism in ICB-resistant melanoma cells.

The inflammatory phenotypes we identify have implications for future rational development of new immunotherapy strategies for patients with AR. Most notably, immune recruitment and infiltration did not appear to be the primary biologic challenges, which provide credence to strategies aimed to reprogram and rescue native anti-tumor immunity. Delivery of *de novo* anti-tumor immunity via engineered antigen-specific cellular or T cell receptor-based therapies<sup>45–49</sup> also appears well-suited to exploit the lack of barriers to immune trafficking and persistent tumor antigen expression. Supporting this hypothesis, we have reported notable responses among patients in this population.<sup>46,50</sup> We are also exploring strategies to interrupt persistent IFN $\gamma$

signaling to reinvigorate immune function and immune checkpoint inhibitor activity in tumors resistant to ICB.<sup>51</sup> While we did observe a few instances of sub-clonal/clonal neoantigen loss, these changes were relatively uncommon and mutation burden was generally unchanged pre- vs. post-treatment.

One potential limitation of our clinical cohort is that it relies on bulk exome and transcriptome data which are prone to be affected by tumor purity. Due to constraints associated with sample purity, we were unable to accurately analyze copy number or loss of heterozygosity. Furthermore, IFN $\gamma$  groupings were only possible for patients with paired pre- and post-progression samples because they were determined relative to each individual. Interestingly, recent analyses utilizing single-cell multi-omics have demonstrated enrichment of CD8<sup>+</sup> T cell exhaustion in the setting of AR to PD-1 blockade in samples from two patients, similar to the exhausted CD8<sup>+</sup> T cells we found in our lung cancer mouse model.<sup>52</sup> Future efforts incorporating single cell multi-omics will be important to parse cancer cell-intrinsic vs. immune or stromally related mechanisms of resistance. Our analysis is limited to correlational observations and focused on PD-1 immunotherapy and not on PD-1 and chemotherapy combination. Although this is now a routine treatment regimen, it is complicated by the uncertainty of contributions of components both to response and to resistance, so for the moment, we have excluded analyses of samples from these patients.<sup>53</sup> Further, heterogeneity in the duration and depth of response to PD-1 blockade in the clinical cohort could not be explored deeper in our molecular cohort due to small sample sizes. Future work is needed to both address heterogeneity in response to mono-therapy with ICB as well as resistance to combinations of chemotherapy and immunotherapy regimens.

Our work informs and builds upon the prior pre-clinical and translational data supporting the intricate role of IFN $\gamma$  in sensitivity and resistance to immunotherapy. Whereas initial IFN $\gamma$  exposure may be fundamental to T cell activation and a hallmark of immune response, persistent IFN $\gamma$  related effects and upregulation may potentially signal immune dysfunction<sup>14,15</sup> and IFN $\gamma$  insensitivity.<sup>13,16,54</sup> In contrast to previous reports linking IFN $\gamma$  insensitivity to mutations in the JAK-STAT pathway, we did not identify specific defects in the IFN $\gamma$  signaling pathway to explain the dysfunctional nature of IFN $\gamma$  response observed in a subset of patient samples. While we found some evidence of B2M and other AP alterations, these changes were predominantly sub-clonal and generally co-occurred in tumors with upregulation of IFN $\gamma$  potentially suggesting they may be an evolutionary consequence rather than an initiating cause of resistance. We have previously shown that chronic IFN $\gamma$  signaling may trigger a cascade of epigenetic modifications in tumor cells including enhanced ISGs and ultimately generate a feedback loop of innate and adaptive immune exhaustion and dysfunction.<sup>14,15</sup> Across multiple murine models of acquired resistance presented here, we recapitulate how acquired resistance is associated with upregulated cancer-intrinsic IFN $\gamma$  response and ultimately tumor insensitivity to effective anti-tumor immunity. Separately, we also show that pre-treatment exposure with IFN $\gamma$  *in vitro* leads to resistance *in vivo* to ICB treatment. Furthermore, we preliminarily observe that *in vivo* generated acquired resistant cell lines in general have altered ISG response as IFN $\gamma$  stimulation *in vitro*



is associated with relatively lower activation of ISGs compared to parental cells stimulated with IFN $\gamma$ . Further work is needed to identify the specific mechanistic deficits in response to the dynamics of IFN $\gamma$  signaling in both immune cells and tumor cells. Overall, these data can further guide more rationally guided therapeutic strategies to prevent, overcome, and reverse AR to PD-1 blockade for patients with lung cancer.

## STAR★METHODS

Detailed methods are provided in the online version of this paper and include the following:

- **KEY RESOURCES TABLE**
- **RESOURCE AVAILABILITY**
  - Lead contact
  - Materials availability
  - Data and code availability
- **EXPERIMENTAL MODEL AND STUDY PARTICIPANT DETAILS**
  - Clinical cohort
  - Study 06
  - Animal models
  - Cell lines
- **METHOD DETAILS**
  - Generation of the molecular dataset from MSK cohort
  - Gene expression profiling from MSK cohort
  - Estimation of gene set enrichment scores from expression data
  - Pseudotime analysis
  - Whole exome sequencing of MSK cohort
  - Tumor heterogeneity and clonality
  - Estimation of somatic signatures in tumor exome data
  - Analysis of selection pressure in mutation data
  - Phylogeny tree reconstruction
  - Neoantigen prediction and fitness score
  - Study 06 sample cohort and transcriptomic analysis
  - Generation of anti-PD-1 resistant CT26 tumors
  - Transcriptomic and ATAC-Seq profiling of anti-PD-1 resistant CT26 cell lines
  - Generation of anti-PD-1 resistant MC38 tumors
  - Gene expression profiling of anti-PD-1 resistant MC38 cell lines
  - Generation of LLC1 and KP tumor cell lines
  - Generation and analysis of RNA-seq of sorted mouse tumor cells
  - *In vivo* mouse lymphocyte studies in LLC1 mouse model
  - Flow cytometry feature clustering
- **QUANTIFICATION AND STATISTICAL ANALYSIS**

## SUPPLEMENTAL INFORMATION

Supplemental information can be found online at <https://doi.org/10.1016/j.ccell.2023.12.013>.

## ACKNOWLEDGMENTS

M.D.H. and this research are supported in part by the Damon Runyon Cancer Research Foundation (grant CI-98-18), the Memorial Sloan Kettering

Cancer Center (support grant/core grant P30 CA008748), Stand Up to Cancer (SU2C)-American Cancer Society Lung Cancer Dream Team Translational research grant (SU2C-AACR-DT17-15), and by The Mark Foundation For Cancer Research (Grant # 19-029 MIA). SU2C is a program of the Entertainment Industry Foundation. Research grants are administered by the American Association for Cancer Research, the scientific partner of SU2C. D.M. was a fellow of the joint EMBL-EBI and NIHR Cambridge Biomedical Research Centre Postdoctoral (EBPOD) program when part of this work was conducted. B.D.G. was supported by an NIH/NCI Cancer Center Support Grant P30 CA008748 and an ASPIRE award from the Mark Foundation. M.L.M. was supported by a Cancer Research UK core grant (C14303/A17197). A.J.M. was supported by The Mark Foundation For Cancer Research, Parker Institute for Cancer Immunotherapy and Breast Cancer Research Foundation. D.Y. and D.M. were supported by the Parker Institute for Cancer Immunotherapy.

## AUTHOR CONTRIBUTIONS

Conceptualization, M.D.H. and M.L.M.; methodology, M.D.H., M.L.M., A.J.M., D.M., A.J.S., D.Y., G.F., and H.R.; investigation, M.D.H., M.L.M., A.J.M., D.M., A.J.S., D.Y., G.F., H.R., X.Z., M.R.K., D.M., K.J.Y., J.Q., J.L., J.M., J.L.S., J.L., A.C., U.K.B., C.M., C.M.V., C.L., M.A., A.J.P., N.M., M.L., B.D.G., T.M., I.A., J.C.B., R.S., P.B., and T.H.S.; writing – original draft, D.M., A.J.S., D.Y., G.F., H.R., M.D.H., M.L.M., and A.J.M.; writing – review & editing, M.D.H., M.L.M., A.J.M., D.M., A.J.S., D.Y., G.F., H.R., X.Z., M.R.K., D.M., K.J.Y., J.Q., J.L., J.M., J.L.S., J.L., A.C., U.K.B., C.M., C.M.V., C.L., M.A., A.J.P., N.M., M.L., B.D.G., T.M., I.A., J.C.B., R.S., P.B., and T.H.S.; funding acquisition, M.D.H., M.L.M., and A.J.M.; resources, M.D.H., M.L.M., A.J.M., D.M., A.J.S., D.Y., G.F., H.R., X.Z., M.R.K., D.M., K.J.Y., J.Q., J.L., J.M., J.L.S., J.L., A.C., U.K.B., C.M., C.M.V., C.L., M.A., A.J.P., N.M., M.L., B.D.G., T.M., I.A., J.C.B., R.S., P.B., and T.H.S.; supervision, M.D.H., M.L.M., and A.J.M.

## DECLARATION OF INTERESTS

A.J.S. reports consulting/advising role to J&J, KSQ therapeutics, BMS, Merck, Enara Bio, Perceptive Advisors, Oppenheimer and Co, Umoja Biopharma, Legend Biotech, Iovance Biotherapeutics, Prelude Therapeutics, Immunocore, Lyell Immunopharma, Amgen and Heat Biologics. Research funding: GSK (Inst), PACT pharma (Inst), Iovance Biotherapeutics (Inst), Achilles therapeutics (Inst), Merck (Inst), BMS (Inst), Harpoon Therapeutics (Inst) and Amgen (Inst). MDH reports research grant from BMS; personal fees from Achilles; Arcus; AstraZeneca; Blueprint; BMS; Genentech/Roche; Genzyme/Sanofi, Immunai; Instil Bio; Janssen; Merck; Mirati; Natera; Nektar; Pact Pharma; Regeneron; Shattuck Labs; Syndax; as well as equity options from Arcus, Factorial, Immunai, and Shattuck Labs. A patent filed by Memorial Sloan Kettering related to the use of tumor mutational burden to predict response to immunotherapy (PCT/US2015/062208) is pending and licensed by PGDx. J.L. has received honoraria from Targeted Oncology and Physicians' Education Resource. D.M. is an employee of M:M Bio Limited. D.M. reports consulting role to Shattuck Labs and Corbus Pharma. T.M. is a consultant for Daiichi Sankyo Co, Leap Therapeutics, Immunos Therapeutics, and Pfizer, and co-founder of Imvax Therapeutics. T.M. has equity in Imvax therapeutics. T.M. reports grants from Bristol Myers Squibb, Surface Oncology, Kyn Therapeutics, Infinity Pharmaceuticals, Peregrine Pharmaceuticals, Adaptive Biotechnologies, Leap Therapeutics, and Aprea. T.M. is an inventor on patent applications related to work on oncolytic viral therapy, alphavirus-based vaccines, neo-antigen modeling, CD40, GITR, OX40, PD-1, and CTLA-4. B.D.G. has received honoraria for speaking engagements from Merck, Bristol Meyers Squibb, and Chugai Pharmaceuticals; has received research funding from Bristol Meyers Squibb and Merck; and has been a compensated consultant for Darwin Health, Merck, PMV Pharma, Shennon Biotechnologies, and Rome Therapeutics of which he is a co-founder. B.D.G. is part of a patent related to neoantigen prediction (WO2018136664A1, PCT/US2023/011643). G.F. and T.H.S. are employees and stockholders of Shattuck Labs, Inc. M.L.M. has received honorarium from GSK. H.R., X.Z., M.R.K., I.A., R.S., J.C.B., M.L.M., and M.D.H. are current employees and stockholders of AstraZeneca.

Received: November 11, 2021  
Revised: September 13, 2023  
Accepted: December 13, 2023  
Published: January 11, 2024

## REFERENCES

- Gandhi, L., Rodríguez-Abreu, D., Gadgeel, S., Esteban, E., Felip, E., De Angelis, F., Domine, M., Clingan, P., Hochmair, M.J., Powell, S.F., et al. (2018). Pembrolizumab plus Chemotherapy in Metastatic Non-Small-Cell Lung Cancer. *N. Engl. J. Med.* 378, 2078–2092.
- Reck, M., Rodríguez-Abreu, D., Robinson, A.G., Hui, R., Csőszi, T., Fülöp, A., Gottfried, M., Peled, N., Tafreshi, A., Cuffe, S., et al. (2016). Pembrolizumab versus Chemotherapy for PD-L1-Positive Non-Small-Cell Lung Cancer. *N. Engl. J. Med.* 375, 1823–1833.
- Schoenfeld, A.J., and Hellmann, M.D. (2020). Acquired Resistance to Immune Checkpoint Inhibitors. *Cancer Cell* 37, 443–455.
- Abdallah, N., Nagasaka, M., Abdulfatah, E., Shi, D., Wozniak, A.J., and Sukari, A. (2018). Non-small cell to small cell lung cancer on PD-1 inhibitors: two cases on potential histologic transformation. *Lung Cancer* 9, 85–90.
- Anagnostou, V., Smith, K.N., Forde, P.M., Niknafs, N., Bhattacharya, R., White, J., Zhang, T., Adleff, V., Phallen, J., Wali, N., et al. (2017). Evolution of Neoantigen Landscape during Immune Checkpoint Blockade in Non-Small Cell Lung Cancer. *Cancer Discov.* 7, 264–276.
- Ascierto, P.A., and McArthur, G.A. (2017). Checkpoint inhibitors in melanoma and early phase development in solid tumors: what's the future? *J. Transl. Med.* 15, 173.
- George, S., Miao, D., Demetri, G.D., Adeegbe, D., Rodig, S.J., Shukla, S., Lipschitz, M., Amin-Mansour, A., Raut, C.P., Carter, S.L., et al. (2017). Loss of PTEN Is Associated with Resistance to Anti-PD-1 Checkpoint Blockade Therapy in Metastatic Uterine Leiomyosarcoma. *Immunity* 46, 197–204.
- Gettlinger, S., Choi, J., Hastings, K., Truini, A., Datar, I., Sowell, R., Wurtz, A., Dong, W., Cai, G., Melnick, M.A., et al. (2017). Impaired HLA Class I Antigen Processing and Presentation as a Mechanism of Acquired Resistance to Immune Checkpoint Inhibitors in Lung Cancer. *Cancer Discov.* 7, 1420–1435.
- Iams, W.T., Shiuan, E., Meador, C.B., Roth, M., Bordeaux, J., Vaupel, C., Boyd, K.L., Summitt, I.B., Wang, L.L., Schneider, J.T., et al. (2019). Improved Prognosis and Increased Tumor-Infiltrating Lymphocytes in Patients Who Have SCLC With Neurologic Paraneoplastic Syndromes. *J. Thorac. Oncol.* 14, 1970–1981.
- Koyama, S., Akbay, E.A., Li, Y.Y., Herter-Sprie, G.S., Buczkowski, K.A., Richards, W.G., Gandhi, L., Redig, A.J., Rodig, S.J., Asahina, H., et al. (2016). Adaptive resistance to therapeutic PD-1 blockade is associated with upregulation of alternative immune checkpoints. *Nat. Commun.* 7, 10501.
- Le, D.T., Durham, J.N., Smith, K.N., Wang, H., Bartlett, B.R., Aulakh, L.K., Lu, S., Kemberling, H., Wilt, C., Lubner, B.S., et al. (2017). Mismatch repair deficiency predicts response of solid tumors to PD-1 blockade. *Science* 357, 409–413.
- Sade-Feldman, M., Jiao, Y.J., Chen, J.H., Rooney, M.S., Barzily-Rokni, M., Eliane, J.-P., Bjorgaard, S.L., Hammond, M.R., Vitzthum, H., Blackmon, S.M., et al. (2017). Resistance to checkpoint blockade therapy through inactivation of antigen presentation. *Nat. Commun.* 8, 1136.
- Zaretsky, J.M., Garcia-Diaz, A., Shin, D.S., Escuin-Ordinas, H., Hugo, W., Hu-Lieskova, S., Torrejon, D.Y., Abril-Rodriguez, G., Sandoval, S., Barthly, L., et al. (2016). Mutations Associated with Acquired Resistance to PD-1 Blockade in Melanoma. *N. Engl. J. Med.* 375, 819–829.
- Benci, J.L., Xu, B., Qiu, Y., Wu, T.J., Dada, H., Twyman-Saint Victor, C., Cuculo, L., Lee, D.S.M., Pauken, K.E., Huang, A.C., et al. (2016). Tumor Interferon Signaling Regulates a Multigenic Resistance Program to Immune Checkpoint Blockade. *Cell* 167, 1540–1554.e12.
- Benci, J.L., Johnson, L.R., Choa, R., Xu, Y., Qiu, J., Zhou, Z., Xu, B., Ye, D., Nathanson, K.L., June, C.H., et al. (2019). Opposing Functions of Interferon Coordinate Adaptive and Innate Immune Responses to Cancer Immune Checkpoint Blockade. *Cell* 178, 933–948.e14.
- Grasso, C.S., Tsoi, J., Onyshchenko, M., Abril-Rodriguez, G., Ross-Macdonald, P., Wind-Rotolo, M., Champhekar, A., Medina, E., Torrejon, D.Y., Shin, D.S., et al. (2020). Conserved Interferon- $\gamma$  Signaling Drives Clinical Response to Immune Checkpoint Blockade Therapy in Melanoma. *Cancer Cell* 38, 500–515.e3.
- Gettlinger, S.N., Wurtz, A., Goldberg, S.B., Rimm, D., Schalper, K., Kaech, S., Kavathas, P., Chiang, A., Lilienbaum, R., Zelterman, D., et al. (2018). Clinical Features and Management of Acquired Resistance to PD-1 Axis Inhibitors in 26 Patients With Advanced Non-Small Cell Lung Cancer. *J. Thorac. Oncol.* 13, 831–839.
- Hänzelmann, S., Castelo, R., and Guinney, J. (2013). GSVA: gene set variation analysis for microarray and RNA-seq data. *BMC Bioinf.* 14, 7.
- Liberzon, A., Birger, C., Thorvaldsdóttir, H., Ghandi, M., Mesirov, J.P., and Tamayo, P. (2015). The Molecular Signatures Database (MSigDB) hallmark gene set collection. *Cell Syst.* 1, 417–425.
- Jiménez-Sánchez, A., Cybulska, P., Mager, K.L., Koplev, S., Cast, O., Couturier, D.-L., Memon, D., Selenica, P., Nikolovski, I., Mazaheri, Y., et al. (2020). Unraveling tumor-immune heterogeneity in advanced ovarian cancer uncovers immunogenic effect of chemotherapy. *Nat. Genet.* 52, 582–593.
- Newman, A.M., Liu, C.L., Green, M.R., Gentles, A.J., Feng, W., Xu, Y., Hoang, C.D., Diehn, M., and Alizadeh, A.A. (2015). Robust enumeration of cell subsets from tissue expression profiles. *Nat. Methods* 12, 453–457.
- Gao, J., Shi, L.Z., Zhao, H., Chen, J., Xiong, L., He, Q., Chen, T., Roszik, J., Bernatchez, C., Woodman, S.E., et al. (2016). Loss of IFN- $\gamma$  Pathway Genes in Tumor Cells as a Mechanism of Resistance to Anti-CTLA-4 Therapy. *Cell* 167, 397–404.e9.
- Rosenberg, J.E., Hoffman-Censits, J., Powles, T., van der Heijden, M.S., Balar, A.V., Necchi, A., Dawson, N., O'Donnell, P.H., Balmanoukian, A., Loriot, Y., et al. (2016). Atezolizumab in patients with locally advanced and metastatic urothelial carcinoma who have progressed following treatment with platinum-based chemotherapy: a single-arm, multicentre, phase 2 trial. *Lancet Lond. Engl.* 387, 1909–1920.
- Miller, B.C., Sen, D.R., Al Abosy, R., Bi, K., Virkud, Y.V., LaFleur, M.W., Yates, K.B., Lako, A., Felt, K., Naik, G.S., et al. (2019). Subsets of exhausted CD8<sup>+</sup> T cells differentially mediate tumor control and respond to checkpoint blockade. *Nat. Immunol.* 20, 326–336.
- Sanchez-Vega, F., Mina, M., Armenia, J., Chatila, W.K., Luna, A., La, K.C., Dimitriadou, S., Liu, D.L., Kantheti, H.S., Saghaforinia, S., et al. (2018). Oncogenic Signaling Pathways in The Cancer Genome Atlas. *Cell* 173, 321–337.e10.
- Campbell, K.R., and Yau, C. (2018). Uncovering pseudotemporal trajectories with covariates from single cell and bulk expression data. *Nat. Commun.* 9, 2442.
- Twyman-Saint Victor, C., Rech, A.J., Maity, A., Rengan, R., Pauken, K.E., Stelekati, E., Benci, J.L., Xu, B., Dada, H., Odorizzi, P.M., et al. (2015). Radiation and dual checkpoint blockade activate non-redundant immune mechanisms in cancer. *Nature* 520, 373–377.
- Sade-Feldman, M., Yizhak, K., Bjorgaard, S.L., Ray, J.P., de Boer, C.G., Jenkins, R.W., Lieb, D.J., Chen, J.H., Frederick, D.T., Barzily-Rokni, M., et al. (2018). Defining T Cell States Associated with Response to Checkpoint Immunotherapy in Melanoma. *Cell* 175, 998–1013.e20.
- Rizvi, N.A., Hellmann, M.D., Snyder, A., Kvistborg, P., Makarov, V., Havel, J.J., Lee, W., Yuan, J., Wong, P., Ho, T.S., et al. (2015). Cancer immunology. Mutational landscape determines sensitivity to PD-1 blockade in non-small cell lung cancer. *Science* 348, 124–128.
- Rizvi, N.A., Cho, B.C., Reinmuth, N., Lee, K.H., Luft, A., Ahn, M.-J., van den Heuvel, M.M., Cobo, M., Vicente, D., Smolin, A., et al. (2020). Durvalumab With or Without Tremelimumab vs Standard Chemotherapy in First-Line Treatment of Metastatic Non-Small Cell Lung Cancer: The MYSTIC Phase 3 Randomized Clinical Trial. *JAMA Oncol.* 6, 661–674.

31. Strickler, J.H., Hanks, B.A., and Khasraw, M. (2021). Tumor Mutational Burden as a Predictor of Immunotherapy Response: Is More Always Better? *Clin. Cancer Res.* 27, 1236–1241.
32. Campbell, J.D., Alexandrov, A., Kim, J., Wala, J., Berger, A.H., Pedamallu, C.S., Shukla, S.A., Guo, G., Brooks, A.N., Murray, B.A., et al. (2016). Distinct patterns of somatic genome alterations in lung adenocarcinomas and squamous cell carcinomas. *Nat. Genet.* 48, 607–616.
33. Skoulidis, F., Goldberg, M.E., Greenawalt, D.M., Hellmann, M.D., Awad, M.M., Gainor, J.F., Schrock, A.B., Hartmaier, R.J., Trabucco, S.E., Gay, L., et al. (2018). STK11/LKB1 Mutations and PD-1 Inhibitor Resistance in KRAS-Mutant Lung Adenocarcinoma. *Cancer Discov.* 8, 822–835.
34. Alexandrov, L.B., Nik-Zainal, S., Wedge, D.C., Aparicio, S.A.J.R., Behjati, S., Biankin, A.V., Bignell, G.R., Bolli, N., Borg, A., Børresen-Dale, A.L., et al. (2013). Signatures of mutational processes in human cancer. *Nature* 500, 415–421.
35. Wang, S., Jia, M., He, Z., and Liu, X.-S. (2018). APOBEC3B and APOBEC mutational signature as potential predictive markers for immunotherapy response in non-small cell lung cancer. *Oncogene* 37, 3924–3936.
36. Martincorena, I., Raine, K.M., Gerstung, M., Dawson, K.J., Haase, K., Van Loo, P., Davies, H., Stratton, M.R., and Campbell, P.J. (2017). Universal Patterns of Selection in Cancer and Somatic Tissues. *Cell* 171, 1029–1041.e21.
37. Jiménez-Sánchez, A., Cast, O., and Miller, M.L. (2019). Comprehensive Benchmarking and Integration of Tumor Microenvironment Cell Estimation Methods. *Cancer Res.* 79, 6238–6246.
38. Zhong, W., Myers, J.S., Wang, F., Wang, K., Lucas, J., Rosfjord, E., Lucas, J., Hooper, A.T., Yang, S., Lemon, L.A., et al. (2020). Comparison of the molecular and cellular phenotypes of common mouse syngeneic models with human tumors. *BMC Genom.* 21, 2.
39. Qiu, J., Xu, B., Ye, D., Ren, D., Wang, S., Benci, J.L., Xu, Y., Ishwaran, H., Beltra, J.-C., Wherry, E.J., et al. (2023). Cancer cells resistant to immune checkpoint blockade acquire interferon-associated epigenetic memory to sustain T cell dysfunction. *Nat. Can. (Ott.)* 4, 43–61.
40. Schroder, K., Hertzog, P.J., Ravasi, T., and Hume, D.A. (2004). Interferon-gamma: an overview of signals, mechanisms and functions. *J. Leukoc. Biol.* 75, 163–189.
41. Efremova, M., Rieder, D., Klepsch, V., Charoentong, P., Finotello, F., Hackl, H., Hermann-Kleiter, N., Löwer, M., Baier, G., Krogsdam, A., and Trajanoski, Z. (2018). Targeting immune checkpoints potentiates immunoeediting and changes the dynamics of tumor evolution. *Nat. Commun.* 9, 32.
42. Peng, W., Chen, J.Q., Liu, C., Malu, S., Creasy, C., Tetzlaff, M.T., Xu, C., McKenzie, J.A., Zhang, C., Liang, X., et al. (2016). Loss of PTEN Promotes Resistance to T Cell-Mediated Immunotherapy. *Cancer Discov.* 6, 202–216.
43. Verdegaa, E.M.E., de Miranda, N.F.C.C., Visser, M., Harryvan, T., van Buuren, M.M., Andersen, R.S., Hadrup, S.R., van der Minne, C.E., Schotte, R., Spits, H., et al. (2016). Neoantigen landscape dynamics during human melanoma-T cell interactions. *Nature* 536, 91–95.
44. Jaiswal, A.R., Liu, A.J., Pudakalakatti, S., Dutta, P., Jayaprakash, P., Bartkowiak, T., Ager, C.R., Wang, Z.-Q., Reuben, A., Cooper, Z.A., et al. (2020). Melanoma Evolves Complete Immunotherapy Resistance through the Acquisition of a Hypermetabolic Phenotype. *Cancer Immunol. Res.* 8, 1365–1380.
45. Samaik, A.A., Hamid, O., Khushalani, N.I., Lewis, K.D., Medina, T., Kluger, H.M., Thomas, S.S., Domingo-Musibay, E., Pavlick, A.C., Whitman, E.D., et al. (2021). Lifleucel, a Tumor-Infiltrating Lymphocyte Therapy, in Metastatic Melanoma. *J. Clin. Oncol.* 39, 2656–2666.
46. Creelan, B.C., Wang, C., Teer, J.K., Tolosa, E.M., Yao, J., Kim, S., Landin, A.M., Mullinax, J.E., Saller, J.J., Saltos, A.N., et al. (2021). Tumor-infiltrating lymphocyte treatment for anti-PD-1-resistant metastatic lung cancer: a phase 1 trial. *Nat. Med.* 27, 1410–1418.
47. D'Angelo, S.P., Mahoney, M.R., Van Tine, B.A., Atkins, J., Milhem, M.M., Jahagirdar, B.N., Antonescu, C.R., Horvath, E., Tap, W.D., Schwartz, G.K., and Streicher, H. (2018). Nivolumab with or without ipilimumab treatment for metastatic sarcoma (Alliance A091401): two open-label, non-comparative, randomised, phase 2 trials. *Lancet Oncol.* 19, 416–426.
48. Doran, S.L., Stevanović, S., Adhikary, S., Gartner, J.J., Jia, L., Kwong, M.L.M., Faquin, W.C., Hewitt, S.M., Sherry, R.M., Yang, J.C., et al. (2019). T-Cell Receptor Gene Therapy for Human Papillomavirus-Associated Epithelial Cancers: A First-in-Human, Phase I/II Study. *J. Clin. Oncol.* 37, 2759–2768.
49. Nagarsheth, N.B., Norberg, S.M., Sinkoe, A.L., Adhikary, S., Meyer, T.J., Lack, J.B., Warner, A.C., Schweitzer, C., Doran, S.L., Korrapati, S., et al. (2021). TCR-engineered T cells targeting E7 for patients with metastatic HPV-associated epithelial cancers. *Nat. Med.* 27, 419–425.
50. Schoenfeld, A., Lee, S., Paz-Ares, L., Doger, B., Gettinger, S., Haefliger, S., Orcurto, A., Sukari, A., Papa, S., Rodriguez Moreno, J.F., et al. (2021). 458 First phase 2 results of autologous tumor-infiltrating lymphocyte (TIL; LN-145) monotherapy in patients with advanced, immune checkpoint inhibitor-treated, non-small cell lung cancer (NSCLC). *J. Immunother. Cancer* 9, A486–A487.
51. Mathew, D., Marmarelis, M.E., Foley, C., Bauml, J.M., Ye, D., Ghinnagow, R., Ngilow, S.F., Klapholz, M., Jun, S., Zhang, Z., et al. (2022). Durable Response and Improved CD8 T Cell Plasticity in Lung Cancer Patients After PD1 Blockade and JAK Inhibition. Preprint at medRxiv. <https://doi.org/10.1101/2022.11.05.22281973>.
52. Pai, J.A., Hellmann, M.D., Sauter, J.L., Mattar, M., Rizvi, H., Woo, H.J., Shah, N., Nguyen, E.M., Uddin, F.Z., Quintanal-Villalonga, A., et al. (2023). Lineage tracing reveals clonal progenitors and long-term persistence of tumor-specific T cells during immune checkpoint blockade. *Cancer Cell* 41, 776–790.e7.
53. Schoenfeld, A.J., Antonia, S.J., Awad, M.M., Felip, E., Gainor, J., Gettinger, S.N., Hodi, F.S., Johnson, M.L., Leighl, N.B., Lovly, C.M., et al. (2021). Clinical definition of acquired resistance to immunotherapy in patients with metastatic non-small-cell lung cancer. *Ann. Oncol.* 32, 1597–1607.
54. Kalbasi, A., Tariveranmoshabad, M., Hakimi, K., Kremer, S., Campbell, K.M., Funes, J.M., Vega-Crespo, A., Parisi, G., Champekar, A., Nguyen, C., et al. (2020). Uncoupling interferon signaling and antigen presentation to overcome immunotherapy resistance due to JAK1 loss in melanoma. *Sci. Transl. Med.* 12, eabb0152.
55. Ritchie, M.E., Phipson, B., Wu, D., Hu, Y., Law, C.W., Shi, W., and Smyth, G.K. (2015). limma powers differential expression analyses for RNA-sequencing and microarray studies. *Nucleic Acids Res.* 43, e47.
56. Garcia-Alonso, L., Holland, C.H., Ibrahim, M.M., Turei, D., and Saez-Rodriguez, J. (2019). Benchmark and integration of resources for the estimation of human transcription factor activities. *Genome Res.* 29, 1363–1375.
57. Jiménez-Sánchez, A., Memon, D., Pourpe, S., Veeraraghavan, H., Li, Y., Vargas, H.A., Gill, M.B., Park, K.J., Zivanovic, O., Konner, J., et al. (2017). Heterogeneous Tumor-Immune Microenvironments among Differentially Growing Metastases in an Ovarian Cancer Patient. *Cell* 170, 927–938.e20.
58. Li, H., and Durbin, R. (2009). Fast and accurate short read alignment with Burrows-Wheeler transform. *Bioinform. Oxf. Engl.* 25, 1754–1760.
59. DePristo, M.A., Banks, E., Poplin, R., Garimella, K.V., Maguire, J.R., Hartl, C., Philippakis, A.A., del Angel, G., Rivas, M.A., Hanna, M., et al. (2011). A framework for variation discovery and genotyping using next-generation DNA sequencing data. *Nat. Genet.* 43, 491–498.
60. Karczewski, K.J., Francioli, L.C., Tiao, G., Cummings, B.B., Alföldi, J., Wang, Q., Collins, R.L., Laricchia, K.M., Ganna, A., Birnbaum, D.P., et al. (2020). The mutational constraint spectrum quantified from variation in 141,456 humans. *Nature* 581, 434–443.
61. Ramos, A.H., Lichtenstein, L., Gupta, M., Lawrence, M.S., Pugh, T.J., Saksena, G., Meyerson, M., and Getz, G. (2015). Oncotator: cancer variant annotation tool. *Hum. Mutat.* 36, E2423–E2429.

62. Mroz, E.A., and Rocco, J.W. (2013). MATH, a novel measure of intratumor genetic heterogeneity, is high in poor-outcome classes of head and neck squamous cell carcinoma. *Oral Oncol.* **49**, 211–215.
63. Roth, A., Khattra, J., Yap, D., Wan, A., Laks, E., Biele, J., Ha, G., Aparicio, S., Bouchard-Côté, A., and Shah, S.P. (2014). PyClone: statistical inference of clonal population structure in cancer. *Nat. Methods* **11**, 396–398.
64. Shen, R., and Seshan, V.E. (2016). FACETS: allele-specific copy number and clonal heterogeneity analysis tool for high-throughput DNA sequencing. *Nucleic Acids Res.* **44**, e131.
65. Gori, K., and Baez-Ortega, A. (2018). Sigfit: Flexible Bayesian Inference of Mutational Signatures (Cancer Biology).
66. Tate, J.G., Bamford, S., Jubb, H.C., Sondka, Z., Beare, D.M., Bindal, N., Boutselakis, H., Cole, C.G., Creatore, C., Dawson, E., et al. (2019). COSMIC: the Catalogue Of Somatic Mutations In Cancer. *Nucleic Acids Res.* **47**, D941–D947.
67. Subramanian, A., Tamayo, P., Mootha, V.K., Mukherjee, S., Ebert, B.L., Gillette, M.A., Paulovich, A., Pomeroy, S.L., Golub, T.R., Lander, E.S., and Mesirov, J.P. (2005). Gene set enrichment analysis: a knowledge-based approach for interpreting genome-wide expression profiles. *Proc. Natl. Acad. Sci. USA* **102**, 15545–15550.
68. Yu, G., Wang, L.-G., Han, Y., and He, Q.-Y. (2012). clusterProfiler: an R package for comparing biological themes among gene clusters. *OMICS A J. Integr. Biol.* **16**, 284–287.
69. Deshwar, A.G., Vembu, S., Yung, C.K., Jang, G.H., Stein, L., and Morris, Q. (2015). PhyloWGS: reconstructing subclonal composition and evolution from whole-genome sequencing of tumors. *Genome Biol.* **16**, 35.
70. Cingolani, P., Platts, A., Wang, L.L., Coon, M., Nguyen, T., Wang, L., Land, S.J., Lu, X., and Ruden, D.M. (2012). A program for annotating and predicting the effects of single nucleotide polymorphisms, SnpEff: SNPs in the genome of *Drosophila melanogaster* strain w1118; iso-2; iso-3. *Fly* **6**, 80–92.
71. Lundegaard, C., Lamberth, K., Harndahl, M., Buus, S., Lund, O., and Nielsen, M. (2008). NetMHC-3.0: accurate web accessible predictions of human, mouse and monkey MHC class I affinities for peptides of length 8–11. *Nucleic Acids Res.* **36**, W509–W512.
72. Vita, R., Mahajan, S., Overton, J.A., Dhanda, S.K., Martini, S., Cantrell, J.R., Wheeler, D.K., Sette, A., and Peters, B. (2019). The Immune Epitope Database (IEDB): 2018 update. *Nucleic Acids Res.* **47**, D339–D343.
73. Altschul, S.F., Gish, W., Miller, W., Myers, E.W., and Lipman, D.J. (1990). Basic local alignment search tool. *J. Mol. Biol.* **215**, 403–410.
74. Łuksza, M., Riaz, N., Makarov, V., Balachandran, V.P., Hellmann, M.D., Soloviyov, A., Rizvi, N.A., Merghoub, T., Levine, A.J., Chan, T.A., et al. (2017). A neoantigen fitness model predicts tumour response to checkpoint blockade immunotherapy. *Nature* **551**, 517–520.
75. Bolger, A.M., Lohse, M., and Usadel, B. (2014). Trimmomatic: a flexible trimmer for Illumina sequence data. *Bioinforma. Oxf. Engl.* **30**, 2114–2120.
76. Dobin, A., Davis, C.A., Schlesinger, F., Drenkow, J., Zaleski, C., Jha, S., Batut, P., Chaisson, M., and Gingeras, T.R. (2013). STAR: ultrafast universal RNA-seq aligner. *Bioinforma. Oxf. Engl.* **29**, 15–21.
77. Liao, Y., Smyth, G.K., and Shi, W. (2019). The R package Rsubread is easier, faster, cheaper and better for alignment and quantification of RNA sequencing reads. *Nucleic Acids Res.* **47**, e47.
78. Şenbabaoğlu, Y., Gejman, R.S., Winer, A.G., Liu, M., Van Allen, E.M., de Velasco, G., Miao, D., Ostrovskaya, I., Drill, E., Luna, A., et al. (2016). Tumor immune microenvironment characterization in clear cell renal cell carcinoma identifies prognostic and immunotherapeutically relevant messenger RNA signatures. *Genome Biol.* **17**, 231.
79. Howe, K.L., Achuthan, P., Allen, J., Allen, J., Alvarez-Jarreta, J., Amode, M.R., Armean, I.M., Azov, A.G., Bennett, R., Bhai, J., et al. (2021). Ensembl 2021. *Nucleic Acids Res.* **49**, D884–D891.
80. Langmead, B., and Salzberg, S.L. (2012). Fast gapped-read alignment with Bowtie 2. *Nat. Methods* **9**, 357–359.
81. Danecek, P., Bonfield, J.K., Liddle, J., Marshall, J., Ohan, V., Pollard, M.O., Whitwham, A., Keane, T., McCarthy, S.A., Davies, R.M., and Li, H. (2021). Twelve years of SAMtools and BCFtools. *GigaScience* **10**, giab008.
82. Zhang, Y., Liu, T., Meyer, C.A., Eeckhoute, J., Johnson, D.S., Bernstein, B.E., Nusbaum, C., Myers, R.M., Brown, M., Li, W., and Liu, X.S. (2008). Model-based analysis of ChIP-Seq (MACS). *Genome Biol.* **9**, R137.
83. Heinz, S., Benner, C., Spann, N., Bertolino, E., Lin, Y.C., Laslo, P., Cheng, J.X., Murre, C., Singh, H., and Glass, C.K. (2010). Simple combinations of lineage-determining transcription factors prime cis-regulatory elements required for macrophage and B cell identities. *Mol. Cell* **38**, 576–589.
84. Frankish, A., Diekhans, M., Jungreis, I., Lagarde, J., Loveland, J.E., Mudge, J.M., Sisu, C., Wright, J.C., Armstrong, J., Barnes, I., et al. (2021). GENCODE 2021. *Nucleic Acids Res.* **49**, D916–D923.
85. Love, M.I., Huber, W., and Anders, S. (2014). Moderated estimation of fold change and dispersion for RNA-seq data with DESeq2. *Genome Biol.* **15**, 550.
86. Jin, H.-T., Anderson, A.C., Tan, W.G., West, E.E., Ha, S.-J., Araki, K., Freeman, G.J., Kuchroo, V.K., and Ahmed, R. (2010). Cooperation of Tim-3 and PD-1 in CD8 T-cell exhaustion during chronic viral infection. *Proc. Natl. Acad. Sci. USA* **107**, 14733–14738.
87. Hudson, W.H., Gensheimer, J., Hashimoto, M., Wieland, A., Valanparambil, R.M., Li, P., Lin, J.-X., Konieczny, B.T., Im, S.J., Freeman, G.J., et al. (2019). Proliferating Transitory T Cells with an Effector-like Transcriptional Signature Emerge from PD-1+ Stem-like CD8+ T Cells during Chronic Infection. *Immunity* **51**, 1043–1058.e4.



# STAR★METHODS

## KEY RESOURCES TABLE

REAGENT or RESOURCE	SOURCE	IDENTIFIER
<b>Antibodies</b>		
BUV395 Rat Anti-Mouse CD44	BD Biosciences	740215; RRID: AB_2739963
BUV496 Rat Anti-Mouse CD45R/B220	BD Biosciences	612950; RRID: AB_2870227
BUV563 Rat Anti-Mouse CD4	BD Biosciences	612923; RRID: AB_2870208
BUV661 Rat Anti-CD11b	BD Biosciences	612977; RRID: AB_2870249
BUV737 Rat Anti-Mouse CD127	BD Biosciences	612841; RRID: AB_2870163
BUV805 Rat Anti-Mouse CD8a	BD Biosciences	612898; RRID: AB_2870186
Brilliant Violet 421™ anti-mouse FOXP3	Biolegend	126419; RRID: AB_2565933
BV480 Mouse Anti-Mouse CD45.2	BD Biosciences	566073; RRID: AB_2739488
BV605 Hamster Anti-Mouse KLRG1	BD Biosciences	564013; RRID: AB_2722497
BV650 Anti-Mouse TCRB	Biolegend	109251; RRID: AB_2810348
BV711 Anti-Mouse CD366 (Tim-3)	Biolegend	119727; RRID: AB_2716208
Brilliant Violet 785™ anti-mouse CD62L Antibody	Biolegend	104440; RRID: AB_2629685
BB700 Ly108	BD Biosciences	742272; RRID: AB_2871448
PE Mouse Anti-TCF-7/TCF-1	BD Biosciences	564217; RRID: AB_2687845
PECy5 CD69	Biolegend	104510; RRID: AB_313113
PECy7 PD1	Biolegend	109110; RRID: AB_572017
TOX Antibody, anti-human/mouse, APC, REAfinity™	Miltenyi	130-118-335; RRID: AB_2751485
Alexa Fluor® 700 anti-mouse/rat/human CD27 Antibody	Biolegend	124240; RRID: AB_2810383
Biotin Anti Mouse CX3CR1	Biolegend	149018; RRID: AB_2565701
eBioscience™ Foxp3 / Transcription Factor Staining Buffer Set	Thermo Fisher	00-5523-00
C57BL/6 WT mice	Charles River Laboratories	Stock 027
CTLA4, Clone: 9H10	BIOXCELL	BE0131; RRID: AB_10950184
PD1, Clone: RMP1-14	BIOXCELL	BE0146; RRID: AB_10949053
CD40, Clone: FGK4.5	BIOXCELL	BE0016-2; RRID: AB_1107601
HLA-1/MHC-1, Clone: A4	eBioscience	14-9958-82; RRID: AB_1210772
B2M Polyclonal	DAKO	A007202; RRID: AB_812325
<b>Biological samples</b>		
Patient tumor tissue from MSKCC Cohort	MSK	–
Patient tumor tissue from Study 06 Cohort	Astra Zeneca	–
CT26 RNA samples for RNAseq	Azenta/Genewiz	–
CT26 DNA samples for ATACseq	Azenta/Genewiz	–
MC38 RNA samples for qPCR	Shattuck Labs	–
KP RNA samples for RNAseq	University of Pennsylvania	–
LLC1 RNA samples for RNAseq	University of Pennsylvania	–
<b>Chemicals, peptides, and recombinant proteins</b>		
Interferon Gamma	R&D Systems	485-MI-100
Collagenase	StemCell Technologies	07902
Venor GeM Mycoplasma Detection Kit	Sigma	MP0025
<b>Critical commercial assays</b>		
First Strand cDNA Synthesis Kit	Origene	NP100042
RNeasy Kit	Qiagen	75144
QIAshredder	Qiagen	79656
RNase-Free DNase Set	Qiagen	79254
SsoAdvanced Universal SYBR Green Supermix	Bio-Rad	1725270

(Continued on next page)

**Continued**

REAGENT or RESOURCE	SOURCE	IDENTIFIER
NextSeq 500/550 v2.5	Illumina	20024906
TruSeq® Stranded Total RNA Library Prep Human/Mouse/Rat (96 Samples)	Illumina	20020597
<b>Deposited data</b>		
Raw Exome data from human clinical samples of MSK Study	This paper	dbGaP Study Accession: phs002834.v1.p1 <a href="https://www.ncbi.nlm.nih.gov/projects/gap/cgi-bin/study.cgi?study_id=phs002834.v1.p1">https://www.ncbi.nlm.nih.gov/projects/gap/cgi-bin/study.cgi?study_id=phs002834.v1.p1</a>
Raw microarray data from human clinical samples of MSK Study	This paper	GEO Accession Number: GSE248249
Raw RNASeq Data from CT26 Mouse Model	This paper	GEO Accession Number: GSE249000
Raw ATACSeq Data from CT26 Mouse Model	This paper	GEO Accession Number: GSE249001
Raw RNASeq Data from LLC1 Mouse Model	This paper	GEO Accession Number: GSE246922
Raw RNASeq Data from KP Mouse Model	This paper	GEO Accession Number: GSE246922
<b>Experimental models: Cell lines</b>		
Mouse CT26 Cell Line	ATCC	ATCC Cat# CRL-2638, RRID: CVCL_7256
Mouse MC38 Cell Lines	License through NCI	RRID: CVCL_B288
Mouse LLC1 Cell Line	ATCC	CRL-1642
Mouse KP Cell Line		N/A
<b>Experimental models: Organisms/strains</b>		
BALB/cJ mice	The Jackson Laboratory	RRID: IMSR_JAX:000651
C57BL/6J mice	The Jackson Laboratory	RRID: IMSR_JAX:000664
<b>Oligonucleotides</b>		
Rps18 Mouse qPCR Primer Pair	Origene	MP212910
Stat1 Mouse qPCR Primer Pair	Origene	MP215434
Stat2 Mouse qPCR Primer Pair	Origene	MP215435
Tap1 Mouse qPCR Primer Pair	Origene	MP217519
Ifitm2 Mouse qPCR Primer Pair	Origene	MP206690
Ifitm3 Mouse qPCR Primer Pair	Origene	MP206691
<b>Software and algorithms</b>		
ImageJ		<a href="https://imagej.nih.gov/ij/">https://imagej.nih.gov/ij/</a>
Illustrator		<a href="https://www.adobe.com">https://www.adobe.com</a>
Python2.7		<a href="https://www.python.org/download/releases/2.7/">https://www.python.org/download/releases/2.7/</a>
R 3.6.1		<a href="https://www.r-project.org">https://www.r-project.org</a>
Bioconductor	R	<a href="https://www.bioconductor.org/">https://www.bioconductor.org/</a>
Deseq2	Bioconductor	<a href="https://bioconductor.org/packages/release/bioc/html/DESeq2.html">https://bioconductor.org/packages/release/bioc/html/DESeq2.html</a>
Trimmomatic v.0.36/v.0.38	Usadel Lab	<a href="http://www.usadellab.org/cms/?page=trimmomatic">http://www.usadellab.org/cms/?page=trimmomatic</a>
Affymetrix Expression Console Software	Affymetrix	<a href="https://www.thermofisher.com/uk/en/home/technical-resources/technical-reference-library/microarray-analysis-support-center.html">https://www.thermofisher.com/uk/en/home/technical-resources/technical-reference-library/microarray-analysis-support-center.html</a>
ComBat	Bioconductor	<a href="https://rdrr.io/bioc/sva/man/ComBat.html">https://rdrr.io/bioc/sva/man/ComBat.html</a>
limma	Bioconductor	<a href="https://bioconductor.org/packages/release/bioc/html/limma.html">https://bioconductor.org/packages/release/bioc/html/limma.html</a>
GSVA package	Bioconductor	<a href="https://bioconductor.org/packages/release/bioc/html/GSVA.html">https://bioconductor.org/packages/release/bioc/html/GSVA.html</a>
PhenoPath	Bioconductor	<a href="https://www.bioconductor.org/packages/release/bioc/html/phenopath.html">https://www.bioconductor.org/packages/release/bioc/html/phenopath.html</a>
bwa aligner v0.7.17	Sanger Institute	<a href="https://github.com/lh3/bwa">https://github.com/lh3/bwa</a>
MATH	Bioconductor	<a href="https://rdrr.io/bioc/maftools/man/math.score.html">https://rdrr.io/bioc/maftools/man/math.score.html</a>

(Continued on next page)



**Continued**

REAGENT or RESOURCE	SOURCE	IDENTIFIER
Oncotator v1	Broad Institute	<a href="https://github.com/broadinstitute/oncotator">https://github.com/broadinstitute/oncotator</a>
Sigfit	University of Cambridge	<a href="https://github.com/kgori/sigfit">https://github.com/kgori/sigfit</a>
dNdScv	Sanger Institute	<a href="https://www.sanger.ac.uk/tool/dndscv/">https://www.sanger.ac.uk/tool/dndscv/</a>
PhyloWGS	Morris Lab	<a href="https://github.com/morrislab/phylowgs">https://github.com/morrislab/phylowgs</a>
NetMHC 3.4	Immune Epitope Database and Analysis Resource	<a href="http://tools.iedb.org/mhci/download/">http://tools.iedb.org/mhci/download/</a>
GSEA R package version 1.2	Broad Institute	<a href="https://rdrr.io/github/GSEA-MSigDB/GSEA_R/">https://rdrr.io/github/GSEA-MSigDB/GSEA_R/</a>
FlowSOM	FlowJo, LLC	<a href="https://bioconductor.org/packages/release/bioc/html/FlowSOM.html">https://bioconductor.org/packages/release/bioc/html/FlowSOM.html</a>
MACS2 2.1.2	Python bioconda	<a href="https://pypi.org/project/MACS2/">https://pypi.org/project/MACS2/</a>
Homer v4.11.1	University of California, San Diego	<a href="http://homer.ucsd.edu/homer/">http://homer.ucsd.edu/homer/</a>
STAR aligner v2.4.0k/v.2.5.2b	Cold Spring Harbor Laboratory,	<a href="https://code.google.com/archive/p/rna-star/">https://code.google.com/archive/p/rna-star/</a>
Bio.pairwise2 package	Biopython	<a href="https://biopython.org/docs/1.75/api/Bio.pairwise2.html">https://biopython.org/docs/1.75/api/Bio.pairwise2.html</a>
CIBERSORT	Stanford University	<a href="https://cibersortx.stanford.edu">https://cibersortx.stanford.edu</a>
GATK v.4.0.2.1	Broad Institute	<a href="https://github.com/broadinstitute/gatk">https://github.com/broadinstitute/gatk</a>
Pyclone-VI	University of British Columbia	<a href="https://github.com/Roth-Lab/pyclone-vi">https://github.com/Roth-Lab/pyclone-vi</a>
snpEff.v4.3t	Wayne State University	<a href="https://pcingola.github.io/SnpEff/">https://pcingola.github.io/SnpEff/</a>
OMIQ	Dotmatics	<a href="https://www.dotmatics.com/solutions/omiq">https://www.dotmatics.com/solutions/omiq</a>
<b>Other</b>		
BioRad CFX Opus 96 and CFX touch 96	Bio-Rad	–

## RESOURCE AVAILABILITY

### Lead contact

Further information and requests for resources and reagents should be directed to and will be fulfilled by the lead contact, Matthew Hellmann ([matt.hellmann@gmail.com](mailto:matt.hellmann@gmail.com)).

### Materials availability

This study did not generate new unique reagents.

### Data and code availability

Microarray expression data from MSK Study Cohort has been deposited in GEO database (GSE248249). Exome sequencing data from MSK Study Cohort has been deposited in dbGaP database (phs002834.v1.p1): [https://www.ncbi.nlm.nih.gov/projects/gap/cgi-bin/study.cgi?study\\_id=phs002834.v1.p1](https://www.ncbi.nlm.nih.gov/projects/gap/cgi-bin/study.cgi?study_id=phs002834.v1.p1). RNA-seq and ATAC-Seq data from CT26 mouse model and RNA-seq data from LLC1 and KP mouse models have been deposited in GEO database (GSE249000; GSE249001; GSE246922) and are publicly available. This paper does not report original code. Any additional information required to reanalyze the data reported in this paper is available from the [lead contact](#) upon request.

## EXPERIMENTAL MODEL AND STUDY PARTICIPANT DETAILS

### Clinical cohort

#### MSK study

Following MSK institutional review board approval, patients with advanced NSCLC treated with PD-(L)1 based therapy between April 2011 and December 2017 were identified. Response Evaluation Criteria in Solid Tumors (RECIST) version 1.1 was used to assess objective response outcomes (n = 1201). Patients with primary resistance were defined as those with progressive disease (PD) at their first on-treatment scan evaluation. Pseudoprogression was excluded from the non-responder group. Patients with AR were defined as those with partial or complete response (PR/CR) followed by isolated or systemic progression on or before the date of their last scan (median follow-up 33.6 months). Post-progression overall survival was calculated from the date of progression on PD-(L)1 inhibitor. Patients who did not die were censored at the date of last contact. A cumulative incidence function with death as a competing risk was used to estimate the proportion of AR over time. Overall survival was estimated using the Kaplan-Meier method. Tumor

tissue samples were obtained with informed consent from patients under protocol #06-107 and #12-245 approved by MSK. This study was approved by the MSK Institutional Review Board and was conducted in accordance with the US Common Rule.

### Study 06

NCT02000947 was a global, non-randomised, open-label, phase 1b study investigating the safety and tolerability of escalating doses of durvalumab in combination with tremelimumab. Subjects were 18 years of age or older, with histologically or cytologically confirmed NSCLC and must have failed to respond to, relapsed following, been ineligible for, or failed to tolerate any line of standard treatment. Patients had to have at least one measurable lesion, with adequate organ and marrow function, and Eastern Cooperative Oncology Group (ECOG) performance status of 0–1. During the initial dose-escalation phase, subjects must not have had prior exposure to immunotherapy. Once the maximum tolerated dose (MTD) or highest protocol-defined dose for each agent in the absence of exceeding the MTD was determined for the immunotherapy-naïve cohort, subjects who had prior exposure to immunotherapy were evaluated. The study was undertaken in accordance with the ethical principles of the Declaration of Helsinki and the International Council on Harmonization guidelines on Good Clinical Practice. The study protocol was reviewed and approved by the Institutional Review Board or Independent Ethics Committee at all participating centers and written informed consent was obtained from all patients. Patients were treated for up to 12 months or until progression or discontinuation due to toxicity. Patients who achieved disease control within the initial 12-month period entered follow-up, and upon evidence of progressive disease were eligible for readministration of treatment provided they had not received additional treatment and continued to meet the protocol defined eligibility criteria.

### Animal models

For CT26 and MC38 models, female inbred BALB/cJ (RRID:IMSR\_JAX000651) or C57BL/6J mice (RRID:IMSR\_JAX:000664), respectively, between 8–12 weeks of age were purchased from The Jackson Laboratory. Mice were housed and acclimated in groups within the internal vivarium for approximately 5–10 days before beginning tumor inoculations. Mice were given a standard diet, allowed free access to water, and were housed on 12-hour light/dark cycles. Animal protocols were approved by an internal Institutional Animal Care and Use Committee (IACUC) and licensed veterinarian. Mice were humanely euthanized through CO<sub>2</sub> asphyxiation followed by cervical dislocation if their tumor volume exceeded 1800mm<sup>3</sup>, there was evidence of severe ulceration at the tumor cell injection site, or if any other significant distress was noted.

All animal experiments for the LLC1 and KP models were performed according to protocols approved by the IACUC of the University of Pennsylvania. Five- to seven-week-old female C57BL/6 (stock# 027) were obtained from Charles River Laboratory. Mice were maintained under specific pathogen free conditions and randomly assigned to each experimental group. Mice were acclimated for 7 days in the vivarium before tumor inoculation. Mice were given a standard diet, allowed free access to water, and were housed on 12-hour light/dark cycles. When tumors reached 15mm in any dimension the mice were euthanized through CO<sub>2</sub> asphyxiation followed by cervical dislocation.

### Cell lines

CT26 colon adenocarcinoma cells (of female origin, RRID:CVCL\_7256) were purchased from ATCC. CT26 cells were cultured in RPMI-1640 media containing 10% fetal bovine serum, 2mM glutamine, 10mM hepes, 1mM sodium pyruvate, 4500 mg/L glucose, 1500 mg/L sodium bicarbonate, and penicillin/streptomycin. Cells were grown at 37°C in a humidified incubator and cell lines in culture were tested monthly using the Venor GeM Mycoplasma Detection Kit (Sigma).

MC38 colon adenocarcinoma cells (of male origin, RRID:B288) were licensed from the National Cancer Institute (NCI). MC38 cells were cultured in Dulbecco's modified MEM with 10% fetal bovine serum, 2mM glutamine, 0.1mM nonessential amino acids, 1mM sodium pyruvate, 10mM Hepes, and penicillin/streptomycin.

LLC1 cells were purchased from ATCC, and KP (Kras mutant P53 mutant) lung cancer cells were a gift from the laboratory of David Feldser. Cells are cultured in GlutaMAX DMEM (DMEM, high glucose, GlutaMAX Supplement, pyruvate, Catalog number: 10569010) in 10% FBS with 100U/mL penn/strep. Cells were passaged every two days and maintained in a 37°C incubator. Chronic IFN cell lines (γKP, γLLC1) were chronically stimulated for 3.5 weeks with 10ng/uL of IFN<sub>γ</sub> (peprotech Catalog Number:315-05) and media replenished every 2 days during splitting, then IFN<sub>γ</sub> washed off and passaged for an additional week before implanting into mice or freezing cell stocks. Resistant cell lines were generated by harvesting late relapse tumors from parental cell lines implanted into mice and treated with immune checkpoint blockade.

## METHOD DETAILS

### Generation of the molecular dataset from MSK cohort

Tumor tissue samples from pre- and post-treatment timepoints were obtained from a subset of patients with NSCLC treated with PD-1 blockade (n = 29). All samples were processed as formalin-fixed paraffin-embedded (FFPE). Sixteen samples were obtained prior to initiation of therapy (pre-treatment) and 37 samples were obtained at time of AR. Most patients had a best overall response of CR or PR per RECIST criteria (n = 22, 76%), with a small subgroup with stable disease (SD, less than 10% tumor shrinkage). Lesion-level response was obtained for all samples (Figure S2). Pre-treatment lesions were those that had at least a 30% reduction in size on treatment or were resected prior to initiating therapy (n = 4). In patients with resected lesion samples, lesion-level response could not be obtained so overall patient-level must have been CR or PR per RECIST. Of note, consistent with prior work demonstrating

generalized inter-tumor uniformity of response, pre-treatment samples derived from resected tumors had similar molecular features of tumors in which the lesion-level response was known (Figure S2). All post-treatment samples were obtained following radiographic progression to PD-1 blockade. Post-treatment samples were defined as “rebound” or “*de novo*” growth (Figure S1A). Rebound lesions were those that were present at initiation of therapy, responded on treatment, but subsequently progressed. *De novo* growth lesions were those that were not present at initiation of therapy and newly grew following treatment. Time to progression in rebound lesions and growth of *de novo* lesions were similar (Figure S1B). Only patients with at least one post-treatment sample were included in this analysis. Samples were molecularly profiled by microarray-based transcriptome sequencing and/or whole exome sequencing. Expression and exome data were available on the same sample for 28 tumor lesions. The following antibodies were used for the immunohistochemistry of the clinical samples: B2M (B2M Polyclonal, DAKO, A0072; RRID: AB\_812325) and HLA (HLA-1/MHC-1, Clone: A4, eBioscience, 14–9958; RRID: AB\_1210772).

### Gene expression profiling from MSK cohort

RNA was extracted from FFPE samples using the RecoverAll Total Nucleic Acid Isolation from Thermo Fisher Scientific (Catalog Number: AM1975). Global RNA expression was measured using the human Affymetrix Clariom D Pico assay. The RNA samples quantification on Affymetrix Arrays was performed in two separate batches. Samples from each batch were processed independently using Affymetrix Expression Console Software. Initially the samples were normalized using the SST-RMA algorithm and outlier samples were excluded. Samples from the two batches were then combined into a single dataset and subject to batch normalization using ComBat. Finally, all the samples were further normalized together using LOESS normalization. For genes with multiple measurements, we selected the measurement with the highest coefficient of variation. The data analysis was focussed on 14,668 annotated protein-coding genes with expression measurements in the arrays. The expression dataset was thoroughly evaluated for technical artifacts such as batch effects (Figure S3A). Differential expression analysis was performed using the limma<sup>55</sup> package in R. Normalized expression data of protein-coding genes were fitted to a linear model using lmFit function and subject to empirical Bayes (eBayes) moderated t-statistics test to identify differentially expressed genes in paired lesions.

### Estimation of gene set enrichment scores from expression data

Enrichment scores were calculated for gene sets from the normalized expression matrix of protein-coding genes using the GSVA package<sup>18</sup> in R with default parameters except for method = ‘ssgsea’ and norm = ‘TRUE’. This approach was used to estimate enrichment scores for the hallmark gene sets (msigdb v6.1 database<sup>19</sup>) and non-redundant cancer and immune-related gene sets in literature. Although clinical data for AR to immunotherapy is fairly limited, recent studies have investigated the impact of chronic ICB treatment in *in vitro* cell lines and *in vivo* settings using mouse models generating either bulk or single-cell RNA-Seq datasets. We manually collated gene sets reported in many of these studies to build an extensive resource of biological processes and gene sets associated with cancer and immune pathways and more specifically ICB resistance (Table S4). In order to select for non-redundant gene sets from this resource, jaccard similarity coefficient was calculated between gene sets based on the number of shared genes and used this metric to perform hierarchical clustering of gene sets and construct a dendrogram with similar gene sets clustering together. Clusters of gene sets were obtained by cutting the dendrogram at a particular level using cutree function in r ( $h = 1.1$ ). A non-redundant list of gene sets was created by selecting one gene set per cluster (Table S4).

Patient samples were classified into ‘increase’ and ‘stable’ sub-groups based on the difference in the enrichment of IFN $\gamma$  response pathway between the paired pre- and post-treatment samples. The ‘increase’ subgroup consisted of samples from patients with differences in scaled enrichment score of IFN $\gamma$  pathway  $>0.025$  while ‘stable’ subgroup was defined by minimal change in enrichment score of IFN $\gamma$  pathway ( $<0.025$  and  $> -0.025$ ). Overlap coefficients were calculated between IFN $\gamma$  gene set and other gene sets to make sure correlation in enrichment score across samples was not driven by shared genes. Change in enrichment score in paired samples was calculated by first scaling the signed enrichment scores values using min-max normalization and then taking the difference in the scaled enrichment scores for paired post and pre-treatment samples for each patient. Enrichment scores were also calculated for transcription factors using the same approach as for other gene sets using previously published regulons of each of the 164 transcription factors.<sup>56</sup> Deconvolution of immune cells from bulk microarray expression data was performed using CIBERSORT<sup>21</sup> tool with default parameters and normalized protein-coding gene expression matrix as input. Significance of change in enrichment score or immune cell estimates for paired samples was calculated using either paired t-test, welch t-test, or wilcoxon signed-rank test depending on the evaluation of equality (Bartlett’s test or Levene’s test) of variance and normality assumptions. All pairwise correlations between gene sets based on change in enrichment scores were performed using spearman’s rank-order correlation method.

### Pseudotime analysis

To decode temporal information that traces the underlying biological process from a cross-sectional cohort of individuals, we applied pseudotime analysis to 13 patients with both pre- and post-treatment gene expression data by using the R package PhenoPath.<sup>26</sup> This analysis assumes that individuals in the cross-sectional cohort behave asynchronously and each is at a different stage of progression. Furthermore, we assumed that the ICB treatment reverses the stage of progression for each individual. Specifically, we used the 500 most variable genes among pre-treatment and 500 most variable genes among post-treatment tumor samples for the pseudotime analysis. Since each subject contributed two gene expression profiles, two covariates (subject and treatment status) were specified in the regression model. To identify the pathways that were associated with pseudotime, we assessed the Spearman

correlations between change in pseudotime and change in ssGSEA enrichment scores of 131 pathways of the hallmark and ICB resistance gene set. To account for multiple testing, we calculated false discovery rate (FDR).

### Whole exome sequencing of MSK cohort

Whole exome sequencing was performed using the Illumina protocol at the Broad Institute of MIT and Harvard, Cambridge, MA, USA using the same protocol as described in Jimenez-Sanchez et al. 2017.<sup>57</sup> Exome samples were aligned to human reference genome (hg19) using bwa aligner (v0.7.17)<sup>58</sup> and the aligned BAM files were subjected to deduplication and base recalibration methods in GATK (v4.0.2.1).<sup>59</sup> These processed BAM files were used for all subsequent analyses. Mutation calling for SNPs and Indels was performed for each tumor-normal (serum) pair using GATK-Mutect2 (v.4.0.2.1) with default parameters and additional filters to remove germline mutations including SNPs detected in gnomAD (Genome Aggregation Database)<sup>60</sup> and mutations in PoN (panel of normal) samples obtained from combining all normal samples in the cohort. Since exome samples were generated in multiple batches with different capture kits (Illumina's Rapid Capture Exome Kit (38Mb target territory), Agilent SureSelect Human All Exon V2 (44Mb target territory), Agilent SureSelect Human All exon V4 (51Mb target territory)), mutations were only called on common regions captured by the three different kits. The mutation calls were annotated using the Oncotator v1<sup>61</sup> tool.

### Tumor heterogeneity and clonality

Tumor heterogeneity was evaluated using the Mutant-Allele Tumor Heterogeneity (MATH) score derived from the variant allele frequencies of somatic mutations as described previously.<sup>62</sup> The clonal population structure of somatic mutations in tumor samples was inferred using Pylone-VI.<sup>63</sup> This method uses a Bayesian statistical approach to estimate cellular prevalence of mutations after accounting for purity of samples. The tumor purity estimates for Pylone-VI were obtained from FACETS<sup>64</sup> and manually corrected for each sample based on the distribution of variant allele frequency. The mean cellular prevalence (MCP) estimates from Pylone-VI were used to classify somatic mutations as clonal (MCP >0.6), sub-clonal (MCP ≤ 0.6) or absent (MCP <0.02).

### Estimation of somatic signatures in tumor exome data

Mutational signatures were estimated using the Sigfit<sup>65</sup> package in R. For each exome sample, the proportion of mutations associated with each of the 30 mutational signatures in the COSMIC<sup>66</sup> database were estimated. Signature 4 corresponds to smoking signature while Signature 13 corresponds to APOBEC signature.

### Analysis of selection pressure in mutation data

Gene-level selection pressure was quantified for pre-treatment and post-treatment samples using the dNdScv<sup>36</sup> package in R. The dNdScv approach quantifies dN/dS ratios based on missense, truncations (nonsense and essential splice site) and indel mutations in a group of samples and identifies genes under positive selection in cancer based on the global p values derived from likelihood tests. Selection pressure was calculated for each gene for pre-treatment and post-treatment samples separately and the difference in selection pressure between the two groups was used to identify potential biologically important genes associated with AR to ICB treatment. Gene sets with significant change in selection pressure between pre- and post-treatment samples were identified via the GSEA<sup>67</sup> approach using the clusterProfiler<sup>68</sup> package in R with the difference in the -log<sub>10</sub>(global p values) between pre- and post-treatment samples, used as a metric to rank genes.

### Phylogeny tree reconstruction

For 12 patients with both pre- and post-treatment whole exome sequencing available, mutations were filtered based on the following criteria: 1) total coverage for tumor ≥ 10, 2) variant allele frequency (VAF) for tumor ≥ 4%, 3) number of reads with alternative allele ≥ 9 for tumor, 4) total coverage for normal ≥ 7, and 5) VAF for normal ≤ 1% at a given mutation. These filters applied to all mutations except for mutations in the KRAS gene. Then pre- and post-therapy mutations were aggregated per patient. PhyloWGS<sup>69</sup> software package (<https://github.com/morrislab/phyloWGS>) was used to infer the clonal structures and estimate clone sizes.

### Neoantigen prediction and fitness score

Filtered mutations were annotated with snpEff.v4.3t software<sup>70</sup> with options set as “-noStats -strict -hgvs1LetterAa -hgvs -canonical -fastaProt [fasta file name]”. All wild-type (WT) and mutant genomic sequences corresponding to coding mutations were translated to an amino acid sequence consistent with the GRCh37 reference genome (GRCh37.75). Only annotations without “WARNING” or “ERROR” were kept and the most deleterious missense mutation was prioritized in mapping a genomic mutation to a gene.

The mutant amino acid from a missense mutation was centered in a 17 amino acids long peptide. Then 9-mers were extracted in a left-to-right sliding fashion. Each mutant 9-mer contained the mutant amino acid on one of the nine positions. In essence, one missense mutation produced up to nine 9-mer peptides. Predictions of MHC class-I binding for both wildtype peptide ( $P^{WT}$ ) and mutant peptide ( $P^{Neo}$ ) were estimated using the NetMHC 3.4<sup>71</sup> software with patient-specific HLA-I types. All  $P^{Neo}$ s with predicted IC50 affinities <500 nM to a patient-specific HLA-I type were defined as neoantigens. Filtered neoantigens were aligned to the known positive epitopes in the Immune Epitope Database<sup>72</sup> (IEDB, <http://www.iedb.org>) for all human infectious disease, class-I restricted targets with positive immune assays using blastp<sup>73</sup> software (<https://blast.ncbi.nlm.nih.gov/Blast.cgi>). We then calculate the alignment scores with the Biopython Bio.pairwise2 package (<http://biopython.org>) for all identified alignments.

Clonal structure, MHC class-I affinities, and epitope alignment scores were put together into the fitness modeling framework in Luksha et al.<sup>74</sup> Neoantigens were mapped to the clonal structure based on the underlying genomic mutations. Then fitness score was calculated for each clone, and the scores were averaged over all the clones in a sample after weighting on clonal sizes.

### Study 06 sample cohort and transcriptomic analysis

Patients enrolled into the Study 06 trial (<https://clinicaltrials.gov/ct2/show/NCT02000947>) were either naïve to ICB treatment or failed on a previous line of anti-PD-(L)1 monotherapy. Those who failed to respond were further categorised as ICB refractory (i.e. primary resistant) or ICB relapsed (i.e. acquired resistant). Patients who were refractory to ICB had documented radiographic disease progression  $\leq 16$  weeks from the start of treatment with no evidence of clinical benefit. Patients who relapsed had radiographic disease progression following initial clinical benefit (i.e., CR, PR, or SD on any scan).

Transcript-per-million (TPM)-normalised RNA-Seq data was available for 26,334 genes in 113 samples from 111 unique patients from Study 06: 58 samples from patients who were ICB-naïve, 28 post-ICB samples from patients who relapsed, and 27 post-ICB samples from patients with refractory disease. The TPM matrix was used as input for ssGSEA as implemented in GSVA R package version 1.42.0 to compute hallmark IFN $\gamma$  signature enrichment scores (ES) in individual samples. ssGSEA ES were compared between samples from patients who relapsed and samples from patients who were ICB naïve or refractory using wilcoxon rank-sum test.

Gene set enrichment analysis (GSEA) from GSEA\_R package version 1.2 was performed on 50 hallmark as well as ConsensusTME immune cell gene sets, using the TPM matrix as input. Briefly, t-tests were run for all 26,334 genes to compare TPM distributions between samples from patients who relapsed and who were ICB naïve or refractory. Genes were then ranked based on t-statistics and GSEA was run on the ranked gene list with 1000 permutations to compute normalised enrichment scores and associated FDR for each gene set. The analysis was run separately for hallmark and ConsensusTME gene sets and volcano plots show combined output of these separate runs.

### Generation of anti-PD-1 resistant CT26 tumors

BALB/C mice were acquired from The Jackson Laboratory, after several days of acclimation, mice were inoculated with 500k CT26 on the rear flank. When the average tumor volume reached 80–100 mm<sup>3</sup> (indicating day 0), mice were given a series of intraperitoneal injections of anti-PD-1 (clone RMP1-14; BioXcell), consisting of 100  $\mu$ g each on days 0, 3, and 6. Tumors were excised from mice that did not respond to anti-PD-1 therapy, approximately 10–14 days following the initial treatment. Tumors were dissociated using collagenase (Stemcell Technologies), washed in 1X PBS, and plated in IMDM culture media supplemented in 10% fetal bovine serum, 1% GLUTiMAX, and 1% Antibiotic-Antimycotic (all GIBCO). Cells were passaged at least 5 times and then inoculated into new recipient mice according to the same protocol as above. Again, when tumors reached 80–100 mm<sup>3</sup>, another treatment course of anti-PD-1 began. This process was repeated for a total of four rounds, at which point none of the treated mice responded to anti-PD-1 therapy. The cell lines generated after two rounds of anti-PD-1 selection are referred to throughout this manuscript as ‘2nd round’, ‘2nd generation’ or ‘F2 generation’, and the cell line generated after four rounds of anti-PD-1 selection are referred to as ‘4th round’, ‘4th generation’, or ‘F4 generation’.

### Transcriptomic and ATAC-Seq profiling of anti-PD-1 resistant CT26 cell lines

Three distinct vials of parental CT26 cells (ATCC; ‘experimental replicates’), two independently isolated tumors from ‘2nd round’ mice, and four independently isolated tumors from ‘4th round’ mice (both ‘biological replicates’), were cultured  $\pm$  20 ng/ml of mouse IFN $\gamma$  (Biolegend) for 24 hours at 37°C/5%CO<sub>2</sub>. The following day, RNA was isolated from cells using Qiagen RNeasy reagents according to manufacturer’s instructions, including QiaShredder homogenization and on-column DNase I digestion. Isolated RNA was sent to Genewiz ([www.genewiz.com](http://www.genewiz.com)) for library generation, RNA-sequencing, and data processing. The NEBNext Ultra II RNA Library Prep Kit for Illumina & NEBNext Poly(A) mRNA Magnetic Isolation Module (New England Biolabs, Ipswich, MA, USA), including clustering and sequencing reagents, was utilized according to the manufacturer’s recommendations. Briefly, mRNAs were initially enriched with Oligod(T) beads. Enriched mRNAs were fragmented for 15 minutes at 94°C. First strand and second strand cDNA were subsequently synthesized. cDNA fragments were end repaired and adenylated at 3’ ends, and universal adapters were ligated to cDNA fragments, followed by index addition and library enrichment by PCR with limited cycles. Briefly, sequencing libraries were generated and sequenced on an Illumina HiSeq (2x150 paired end reads), targeting  $>20 \times 10^6$  reads per sample. Sequences were trimmed using Trimmomatic v.0.36<sup>75</sup> and mapped to *Mus musculus* GRCm38 reference genome using STAR aligner v.2.5.2b.<sup>76</sup> Unique gene hits were calculated by using featureCounts from the Subread package v.1.5.2.<sup>77</sup> Only unique reads that fell in exonic regions were counted. The TPM values were obtained for each protein-coding gene and subsequently log-transformed ( $\log_2(\text{TPM} + 1)$ ) for downstream analysis. Mouse orthologs of genes in hallmark gene sets and antigen processing machinery<sup>78</sup> and regulons of IRF1 and STAT1 were identified using Ensembl v87<sup>79</sup> and ssGSEA was performed in a similar fashion as described for the clinical cohort.

For ATAC-Seq, CT26 cell pellets from two distinct vials of parental CT26 cells, five independently isolated tumors from mice, and five independently isolated tumors from ‘4th round’ mice were collected according to the same procedure as described above for RNA isolation, and pellets were sent to Genewiz ([www.genewiz.com](http://www.genewiz.com)) for nuclei isolation, library generation, and sequencing. Nuclei were treated with Tn5 enzyme (Illumina, Cat. #20034197) for 30 minutes at 37°C and purified with Minelute PCR Purification Kit (Qiagen, Cat. #28004) to produce tagmented DNA samples. Tagmented DNA was barcoded with Nextera Index Kit v2 (Illumina,



Cat. #FC-131-2001) and amplified via PCR prior to a SPRI Bead cleanup to yield purified DNA libraries. ATAC-Seq raw data was trimmed using Trimmomatic 0.38<sup>75</sup> to remove sequencing adapters and low-quality bases. Cleaned reads were next aligned to reference genome mm10 using bowtie2.<sup>80</sup> Aligned reads were filtered using samtools 1.9<sup>81</sup> to keep alignments that have a minimum mapping quality of 30 and are aligned concordantly. Peak calling was performed using MACS2 2.1.2<sup>82</sup> to identify open chromatin regions. For each pair-wise comparison, peaks from the relevant conditions are merged and peaks found in either condition are kept for downstream analyses. Reads falling beneath peaks were counted in all samples, and these counts were used for differential peak analyses using the R package Diffbind. Gene sets with significant change in peak binding between 4<sup>th</sup> generation and control (parental or *in vivo*) cells were identified via the GSEA<sup>67</sup> approach using the clusterProfiler<sup>68</sup> package in R with the mean fold change in peak binding used as a metric to rank genes. Motif analysis was performed using *de novo* motif search in promoter peak regions using findMotifsGenome.pl algorithm (with default parameters) in Homer v4.11.1 software.<sup>83</sup>

### Generation of anti-PD-1 resistant MC38 tumors

Wild-type (WT) MC38 (colorectal carcinoma) cells were acquired by license from the NCI, and were cultured in IMDM media, with 10% FBS, antibiotic/antimycotic, and gentamycin (all GIBCO), and were cultured in an incubator at 37°C with 5% CO<sub>2</sub>. Cell lines in active culture are tested monthly using the Venor GeM Mycoplasma Detection Kit (Sigma). MC38 cells were inoculated (500,000 cells) on the hind flank of C57BL/6 mice (Jackson Laboratories), and when tumors became palpable, mice were either treated with vehicle (PBS) or anti-PD-1 (100 µg of clone RMP1-14 on days 0, 3, and 6 via intraperitoneal injection (IP); BioXCell). Tumor growth was measured over time and after approximately 20 days following the first treatment, tumors were isolated (indicating round 1), dissociated using collagenase (StemCell Technologies), washed in 1X PBS, and plated in culture media. Cells were passaged a minimum of two times and were then used to inoculate new C57BL/6 mice. Again, another course of vehicle or anti-PD-1 was given to the animals, tumor measurements were taken over time, and tumors were isolated approximately 20 days after treatment, from non-responding animals (indicating round 2). This *in vivo* anti-PD-1 selective pressure was performed for a total of five rounds until none of the mice responded to anti-PD-1 therapy. These isolated tumors are referred to throughout as '5th round' and represent the tumor cells used to characterize the MC38 acquired resistance model (MC38/AR).

### Gene expression profiling of anti-PD-1 resistant MC38 cell lines

Cells from four WT (or vehicle treated mice) and four 5th round AR tumors were treated +/- 20 ng/mL mouse IFN $\gamma$  (R&D Systems) for three hours. After three hours, cell culture supernatant was removed and RLT lysis buffer (Qiagen) prepared with 5% 2-mercaptoethanol was added directly to the cells. Following lysis, lysates were homogenized with the Qiagen QIAshredder and RNA was harvested using Qiagen RNeasy columns including on-column DNase I digestion. Then, 1 µg of RNA was reverse transcribed using Origene First Strand cDNA synthesis reagents. cDNA was diluted further with nuclease-free water and qPCR was performed at a series of genes, in triplicate, and SYBR Green signal was assessed on the BioRad CFX Opus 96 and CFX Touch 96. Mouse validated gene primer sequences from Origene were used, and included mouse *Stat1*, *Stat2*, *Tap1*, *Ifitm2*, *Ifitm3*, and the house-keeping control *Rps18*. Fold-change in gene expression at baseline was calculated using the  $\Delta\Delta$ CT method where the first WT tumor sample was set to 1. Each additional gene was compared to this sample and the *Rps18* house-keeping control. Fold-change in IFN $\gamma$  responsiveness was also calculated using the  $\Delta\Delta$ CT method where each IFN $\gamma$  treated tumor samples was normalized to its representative IFN $\gamma$  untreated samples.

### Generation of LLC1 and KP tumor cell lines

Tumor injection and treatment schedule were done as previously described (Twyman-Saint Victor et al., 2015). A single flank was injected per mouse. Antibodies against CTLA-4 (9H10) or PD-1 (RMP1-14) were given on days 4, 7, and 10 for LLC1 and on days 5,8,11 for KP unless otherwise specified. Antibodies against CD40 (FGK4.5/FGK45) were given on Day 11 for KP studies. On day 15, tumors were harvested, red blood cell (RBC) lysis was performed, and a single cell suspension was created. Tumor cells were stained with Live/Dead Aqua and CD45. Samples were sorted on an Aria (BD) by gating on live, CD45 negative cells.

### Generation and analysis of RNA-seq of sorted mouse tumor cells

Total RNA was isolated and purified from the cells using Isol-RNA Lysis Reagent (Fisher) and treated with DNase I (Fisher). RNA-Seq libraries were prepared using the TrueSeq Stranded Total RNA Library Prep Kit (Illumina) and sequenced on Illumina HiSeq 2500 with 100 base paired end reads. Reads were trimmed first using cutadapt v1.9 (<http://code.google.com/p/cutadapt/>) with parameters -q 10 -m 30 -O 4. Trimmed reads that were aligned to rRNAs sequences were removed and the remaining sequences were aligned to the GRCm38 reference genome using STAR v2.4.0k<sup>76</sup> with parameters -outFilterMultimapNmax 100 -outFilterMismatchNmax 999 -outFilterMismatchNoverLmax 0.06. Primary aligned reads were counted against GENCODE<sup>84</sup> annotation vM4 using Subread v1.4.6<sup>77</sup> with parameters -s 2 -minReadOverlap 10. Raw counts were subjected to variance stabilizing transformation (VST) in Deseq2<sup>85</sup> before downstream analysis. Mouse orthologs of genes in Hallmark IFN $\gamma$  signature gene set were identified using Ensembl v87<sup>79</sup> and ssGSEA was performed in a similar fashion as described for the clinical cohort.

### *In vivo* mouse lymphocyte studies in LLC1 mouse model

Tumors, spleens, and draining lymph node (DLN) were harvested at day 16 post tumor implantation. For spleens and DLNs, single-cell suspensions were prepared after RBC lysis with ACK Lysis Buffer (Life Technologies). Tumors were weighed prior to enzymatic



digestion with Type 4 collagenase and DNase I at 1 mg/mL. After enzymatic digestion or ACK Lysis, all tissues were filtered through 100-micron filters. Cells were stained with Fc Block and Zombie Live/Dead stain for 10 minutes prior to surface stain. Surface stain was done for 30 minutes at room temperature. Samples were fixed and permeabilized by incubating in 100  $\mu$ L of Fix/Perm buffer at room temperature for 30 minutes and washed in Perm Buffer. Intracellular stains were performed overnight at 4°C. Cell counting beads were spiked into each sample prior to data acquisition. Data acquisition was done on a FACSymphony A5. See [key resources table](#) for list of antibodies and buffers.

### Flow cytometry feature clustering

For quantification and statistical analysis of flow cytometry data, both OMIQ and custom R scripts were utilized. Manual gating was used to define total CD8<sup>+</sup> T cells and subsets of exhausted CD8<sup>+</sup> T cells among the TILs. Furthermore, 15K CD8<sup>+</sup> T cells were equally sampled from each FCS file and projected into opt-SNE space using OMIQ. FlowSOM clustering identified 12 clusters which was biologically defined based on geometric mean fluorescence intensity levels detailed in the heatmap.<sup>86,87</sup>

### QUANTIFICATION AND STATISTICAL ANALYSIS

All statistical tests were performed in R. Statistical details of individual experiments can be found in the relevant figure legend and results section. For all analyses, p values <0.05 were considered significant.